

DEVELOPMENT OF HIGH POWER FIBER LASER TECHNOLOGIES

Thesis

Submitted to

The School of Engineering of the

UNIVERSITY OF DAYTON

In Partial Fulfillment of the Requirements for

The Degree

Master of Science in Electro-Optics

By

Renjie Zhou

UNIVERSITY OF DAYTON

Dayton, Ohio

May 2010

DEVELOPMENT OF HIGH POWER FIBER LASER TECHNOLOGIES

APPROVED BY

Joseph W. Haus, Ph.D.
Advisor
Professor and Director
Electro-Optics Graduate Program

Qiwen Zhan, Ph.D.
Advisor
Associate Professor
Electro-Optics Graduate Program

Peter E. Powers, Ph.D.
Committee Member
Department of Physics &
Electro-Optics Graduate Program

Malcolm W. Daniels, Ph.D.
Associate Dean
School of Engineering

Tony E. Saliba, Ph.D.
Dean, School of Engineering

© Copyright by

Renjie Zhou

All rights reserved

2010

ABSTRACT

DEVELOPMENT OF HIGH POWER FIBER LASER TECHNOLOGIES

Name: Zhou, Renjie
University of Dayton

Co-advisor: Dr. Joseph W. Haus and Qiwen Zhan

The development of high power fiber laser and technologies are covered in this thesis. The first part of the thesis simulates the signal gain spectrum in an erbium-ytterbium fiber amplifier, which can be implemented in fiber laser systems to generate high power output. The second part proposes the use of gain-guided (GG) optical fibers to achieve high power mode-locked fiber lasers. The spatial-temporal pulse propagation in the GG fiber is simulated; self-focusing, and self-phase-modulation in this type of fiber is studied. The third part discusses phase-locked fiber laser designs. Self-imaging in optical fibers is simulated; the results provide a guide to the phase-locking fiber laser system design.

The last part of the thesis investigates theoretically and experimentally cylindrical vector (CV) beams generation from fiber laser system using a birefringent crystal. Radial and azimuthal polarization output can be switched

easily in this fiber cavity design. More interestingly, lasing with radial and azimuthal polarization can be achieved simultaneously. By introducing misalignment in the cavity, a beam with different polarization distributions is generated.

Dedicated to my parents

ACKNOWLEDGEMENTS

Firstly, I would like to give my thanks to my advisors Drs. Joseph Haus and Qiwen Zhan for their assiduous advising during my M.S degree study. Also, many thanks give to Dr. Peter Powers for instructing me during the experiments, and for answering my questions patiently every time.

At the same time, I appreciate Dr. Baldemar Ibarra-Escamilla for his useful skills with fiber laser experiments.

Also, thanks give to Dr. Zhan's research group members and other EOP students, especially Jean Bosco, Jonathan Evans, and Nkorni Katte.

Besides, I would like to appreciate my friends in China, France, and the united states for their concerning and help to me. Especially, I owe my thanks to Tracy Yang.

Finally, and most importantly, all my achievement gives to my parents for their continuing supporting to my study and daily life.

TABLE OF CONTENTS

ABSTRACT	iv
ACKNOWLEDGEMENTS.....	vii
LIST OF TABLES.....	xi
LIST OF ILLUSTRATIONS.....	xii
CHAPTER	
INTRODUCTION	1
I. Modeling of erbium-ytterbium co-doped fiber amplifier	3
1.1 Introduction of Erbium-Ytterbium fiber amplifier	3
1.2 Erbium-Ytterbium fiber amplifier dynamics	5
1.3 Numerical modeling of signal gain in Er-Yb fiber amplifier	8
1.3.1 Simplification of rate equations.....	8
1.3.2 Pump dissipation and signal gain simulation.....	10
1.4 Summary.....	16
II. Modeling of beam propagation in gain-guided fiber.....	17
2.1 Introduction to gain-guided fiber	17
2.2 Theoretical analysis	19

2.2.1 Modes in gain-guided fiber	19
2.2.2 Nonlinear Schrödinger equation(NLSE)	21
2.2.3 Numerical algorithm solving pulse propagation	22
2.3 Simulation results	26
2.3.1 Self-focusing and collapsing in gain-guided fiber	26
2.3.2 Self-phase modulation in gain-guided fiber	29
2.3.3 Pulse coupling into single mode fiber	30
2.4 Kerr-lens mode-locking with gain-guided fiber.....	34
2.5 Summary	36
III. Development of phase-locking fiber lasers	37
3.1 Self-imaging in waveguides.....	37
3.2 Numerical simulation of self-imaging in fiber	41
3.3 Phase-locking fiber laser design.....	43
3.4 Summary	45
IV. Erbium fiber laser generating Vectorial Beams.....	46
4.1 Introduction and development of Cylindrical Vector Beams	47
4.2 Theoretical analysis.....	50
4.2.1 Fiber modes	50
4.2.2 Birefringence crystal for polarization selection	54
4.3 Experimental generation of Vectorial Beams.....	59
4.3.1 Experimental generation of Cylindrical Vectorial Beams	60

4.3.2 Polarization evolution in fiber laser cavity.....	65
4.3.3 Generation of generalized cylindrical vector output.....	70
4.3.4 Vectorial vortex mode generation with angular misalignment.....	71
4.4 Summary.....	76
V. CONCLUSION AND FUTURE WORK.....	79
BIBLIOGRAPHY.....	82

LIST OF TABLES

Table 1-1. Parameters of the Er/Yb amplifier	11
Table 3-1. The parameter of the multi-mode fiber and the beams coupled into the fiber for self-imaging.....	42

LIST OF ILLUSTRATIONS

Figure 1-1. Energy diagram describes the absorption and transfer in Er–Yb co-doped system.....	5
Figure 1-2. Flow draft of the signal gain and pump dissipation calculation.....	12
Figure 1-3. Up-level population concentration of Erbium.....	13
Figure 1-4. Up-level population concentration of Ytterbium.....	13
Figure 1-5. Pump power dissipation vs. propagation distance.....	14
Figure 1-6. Signal power vs. propagation distance.....	14
Figure 1-7. Signal gain in dB vs. propagation distance.....	15
Figure 2-1. Field amplitudes of the spatial-temporal pulse propagations in GG fiber. (a) is the initial pulse; (b)-(d) correspond to the pulse propagation in the 50 μm core radius of the fiber, and the distances are 10 cm, 11 cm, 11.2cm, respectively; (e)-(g) correspond to the pulse propagation in the 75 μm core radius of the fiber, and the distances are 8.4 cm, 9.0 cm, 9.2cm, respectively; (h)-(j) correspond to the pulse propagation in the 100 μm core radius of the fiber, and the distances are 8.2 cm, 8.8 cm, 9.0cm, respectively.	28
Figure 2-2. On-axis phase evolution for the pulses propagation in the GG fiber. (a) is the phase for the initial pulse; (b)-(d) are the phases corresponding to pulse	

propagation in the 50 μm core radius of the fiber, and the distances are 10 cm, 11 cm, 11.2cm, respectively; (e)-(g) are the phases corresponding to pulse propagation in the 75 μm core radius of the fiber, and the distances are 8.4 cm, 9.0 cm, 9.2cm, respectively; (h)-(j) are the phases corresponding to pulse propagation in the 100 μm core radius of the fiber, and the distances are 8.2 cm, 8.8 cm, 9.0cm, respectively.30

Figure 2-3. GG fiber is spliced to a single mode fiber.....31

Figure 2-4. Power in the single mode fiber versus input power coupled into the GG fiber. (a), (c), and (e) are power the transmission curves for 50 μm , 75 μm , and 100 μm core size respectively, and the GG fiber lengths are 11.2 cm, 9.2 cm, and 9.0 cm accordingly. (b), (d), and (f) are the phase curves for 50 μm , 75 μm , and 100 μm core size respectively.....33

Figure 2-5. Illustration of Kerr-lens mode-locking with GG fiber and SMF fiber device.....34

Figure 3-1. Multimode waveguide with mirror image at $3L_\pi$, direct image at $2(3L_\pi)$, and two fold images at $\frac{1}{2}(3L_\pi)$ and $\frac{3}{2}(3L_\pi)$ 40

Figure 3-2. Illustration of two beams coupled into a multi-mode fiber. The beam centers are located at x_1 and x_2 respectively.....41

Figure 3-3. Self-imaging in MMF. The initial two Gaussian beams formed single self-imaging at about $z=14$ mm, and 2 double self-imaging at about $z=7$ mm....43

Figure 3-4. Phase-locked fiber laser system designs.....43

Figure 3-5. Simulation of self-imaging in LMA fiber of the phase-locking fiber laser system.....44

Figure 4-1. Intensity distributions of the fiber modes of erbium-doped fiber used in the experiment. (a): LP₀₁ mode intensity distribution; (b): LP₁₁ mode intensity distribution. The unit for x, and y axis is μm.....52

Figure 4-2. Intensity and polarization distributions for the degenerated LP₁₁ modes. (a): representation of TE₀₁ mode with azimuthal polarization; (b): representation for the TM₀₁ mode with radial polarization; (c): representation for the hybrid mode with mixed polarization. The polarization distributions are indicated by white arrows. The unit for x, and y axis is μm.....53

Figure 4-3. Illustration of birefringence crystal angular separation of radial and azimuthal polarizations. (a): The ray traces through the birefringence crystal; (b): The index ellipsoid of the calcite crystal. The calcite crystal is negative uniaxial crystal with $n_o=1.633$, and $n_e= 1.478$ at 1.6 μm wavelength.....56

Figure 4-4. Normal surface of the calcite crystal used for describe the wavefront and energy flow directions.....56

Figure4-5. Plot of separation angle of the wavefronts and energy flows for ordinary and extraordinary rays, and the foci separation as a function of incident angle. (a): Plot of the separation and wavefronts and the energy flow, and the walk-off angle as a function of function. The unit of x and y axis is radian; (b): Plot of the foci separation as a function of incident angle. The x axis unit is radian,

and the y axis unit is mm.....58

Figure 4-6. Experiment setup of an Erbium doped fiber laser generating radially or azimuthally polarization. The solid rays indicate ordinary beams (azimuthal polarization), and the dashed rays indicates extraordinary rays (radial polarization).....61

Figure 4-7. Measurements of the azimuthally polarized mode, and linescan comparisons between the experiment and theory. (a): Intensity distribution of the output beam; (b)-(e): intensity distributions after a linear polarizer. The polarizer transmission axis is indicated by white arrows; (f) linescans comparison between the experimental result and the theoretical prediction. The theoretical curve is calculated with a Laguerre Gaussian distribution. The unit of x axis is mm, and the y axis intensity peak is normalized to unity.....63

Figure 4-8. Measurements of the radially polarized mode, and linescan comparisons between the experiment and theory. (a): Intensity distribution of the output beam; (b)-(e): intensity distributions after a linear polarizer. The polarizer transmission axis is indicated by white arrows; (f) linescans comparison between the experimental result and the theoretical prediction. The theoretical curve is calculated with Laguerre-Gaussian distribution. The units of x axis is mm, and the y axis intensity peak is normalized to unity.....63

Figure 4-9. Output power vs. the launched pump power.....64

Figure 4-10. Illustration of the vectorial fiber laser design with a c-cut calcite crystal and a three-lens telescope in the cavity. An example of radial polarization mode intensity generated with this laser is shown at the top right inset photo. A series of four photos after inserting a linear polarizer is short on the top left inset.....65

Figure 4-11. Polarization states between L3 and L4 when the output is radial polarization. (a)-(c) represent the beam from the fiber; (a) the initial the beam from the fiber, (b) and (c) are the beams after a linear polarizer; (d)-(f) represent the beam from the crystal back into the fiber; (d) the initial beam without linear polarizer, (e) and (f) are the beams after a linear polarizer. The linear polarizer axes are indicated by white arrows.....67

Figure 4-12. Polarization states between L3 and L4 when the output is azimuthal polarization. (a)-(c) represent the beam from the fiber; (a) the initial the beam from the fiber, (b) and (c) are the beams after linear polarizers; (d)-(f) represent the beam from the crystal; (d) the initial beam from the crystal, (e) and (f) are the beams after linear polarizers. The linear polarizer axes are indicated by white arrows.....68

Figure 4-13. Polarization states in the cavity in front of M1 for radial and azimuthal polarization outputs. (a)-(c) and (d)-(f) represent the polarization states for radial and azimuthal polarization outputs respectively. The linear polarizer axes are indicated by white arrows.....70

Figure 4-14. Generation of generalized cylindrical vector polarization. (a) the output beam intensity profile; (b)-(e) the intensity profiles after a linear polarizer whose transmission axis is indicated by the white arrows.....71

Figure 4-15. Experimental results of output mode with angular misalignment and four-spot patterns after polarizer. (a) the intensity profile of the output mode; (b)-(e) the beam intensity profiles after a linear polarizer whose transmission axis is indicated by the white arrow.....73

Figure 4-16. Numerical simulation results of the linear superposition of radial and azimuthal polarization with one opposite topological charge. (a) shows the overall intensity profile; (b)-(e) are the beam profiles after linear polarizer whose transmission axis is indicated by white arrows.....74

Figure 4-17. Experimental results of output mode with angular misalignment and six-spot patterns after polarizer. (a) the intensity profile of the output mode; (b)-(e) the beam intensity profiles after a linear polarizer whose transmission axis is indicated by the white arrow.....75

Figure 4-18. Numerical simulation results of the linear superposition of radial and azimuthal polarization with two opposite topological charges. (a) shows the overall intensity profile; (b)-(e) are the beam profiles after linear polarizer whose transmission axis is indicated by white arrows.75

Figure 5-1. Updated fiber laser system design for further improve the slope efficiency.....81

INTRODUCTION

This thesis focuses on the development of high power fiber lasers technologies. The study is based on both numerical simulation and experimental works.

Er-Yb fiber and GG fiber, which are suitable for high power fiber lasers, are introduced. For the Er-Yb fiber amplifier, the signal gain and pump dissipation are computed by solving the rate equations for the system. The results give information on optimization of the fiber laser system for high power output. For the GG fiber, the spatial-temporal pulse propagation is simulated. We studied self-focusing and self-phase modulation in the fiber, and proposed using this fiber device with a single mode fiber for a mode-locked fiber lasers design which is capable of generating short pulses with high peak power.

Besides simulation of signal gain and pulse propagation in the fibers, a phase-locked fiber laser design which can coherently combine fiber laser arrays for high power output is also presented. This system is based on self-imaging effect in Large-Mode-Area (LMA) fibers. In the simulation, four 2-D Gaussian beams are coupled to the LMA fiber, and the evolution of the beam with self-imaging effect is simulated numerically. The simulation results provide a guide

for the cavity design.

Finally, an Er-fiber laser system which can generate radial, azimuthal polarization and generalized cylindrical vector beams is proposed and experimentally demonstrated. The cavity design features the use of a birefringent crystal which provides polarization discrimination. The polarization evolution is investigated, and it is found the fiber acts as a polarization convertor in the cavity. Additionally, more general vector beams are also generated when misalignment of the optical components is introduced in the cavity. This fiber laser provided a CV beam output power that is far beyond the reported record. Possible design strategies that can further improve the output power is also proposed.

CHAPTER I

MODELING OF ERBIUM-YTTERBIUM CO-DOPED FIBER AMPLIFIER

In this chapter, Er-Yb fiber amplifier is introduced including the co-doped system energy levels and rate equations. Then the dynamic rate equations are solved numerically. By solving the rate equations, the pump and signal power evolution in the fiber is obtained.

1.1 Introduction of Erbium-Ytterbium fiber amplifier

Recently, rare-earth doped fiber lasers and amplifiers have attracted increasing interest. These types of fiber amplifier show high gain with high pump efficiency, good beam quality, high reliability, and compactness. Thus, they are find potential applications for fiber communication, remote sensing, medicine, and fabrication.

Among all the rare-earth fiber amplifiers, erbium–ytterbium co-doped fiber amplifiers have received great attention during the past few years. The main reason is its potential application in fiber telecommunication and the generation of high power lasers at $1.55\ \mu\text{m}$ [1, 2]. Compared with an Er-doped fiber amplifier, the co-doping with Yb ions improves the pump absorption significantly while at

the same time, detrimental clustering of Er^{3+} ions is reduced because the Yb^{3+} concentration is normally higher than the Er^{3+} concentration. Thus, with this kind of fiber it is possible to make a short- cavity fiber laser [3]. Recently, Er-Yb fiber lasers with high slope efficiency and high output power have been demonstrated [4].

1.2 Erbium-Ytterbium fiber amplifier dynamics

The Energy level diagram which describes the photo absorption and transfer in Er-Yb co-doped is drawn in Figure 1-1[5]. The pump photons centered

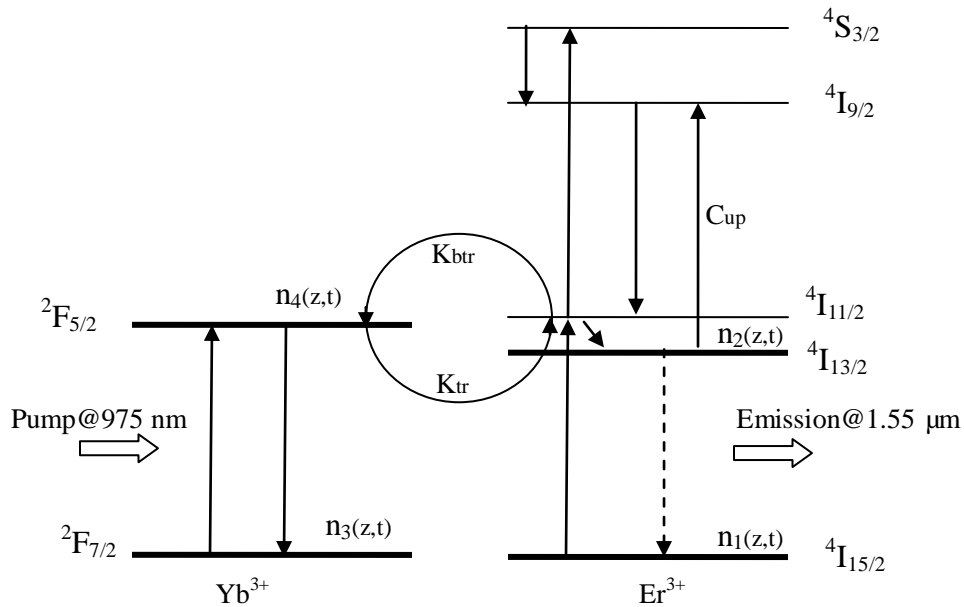


Figure 1-1. Energy diagram describes the absorption and transfer in Er–Yb co-doped system.[5]

at 975 nm are first absorbed by the $^2F_{7/2}$ state of Yb³⁺, exciting the Yb³⁺ ion from the $^2F_{7/2}$ state into the $^2F_{5/2}$ of the Yb³⁺. From there, a cooperative energy transfer process happens that the excited Yb³⁺ ions excite the Er³⁺ ions to the $^4I_{11/2}$ state from the ground state $^4I_{15/2}$ while dropping back Yb³⁺ ions to their ground state $^2F_{7/2}$. This process is described by the energy transfer coefficient k_{tr} . Note that the Er³⁺ ions can also absorb photons around 975 nm, but the absorption efficiency is much lower compared with Yb³⁺.

In order to simplify the rate equations of this co-doped fiber amplifier system, I made some assumptions and give some explanations for the energy level diagram [5-7]. Firstly, we assume that the signal depletion time is much shorter than the upper level lifetime. Secondly, since level ${}^4F_{11/2}$ has a very short lifetime (1 μ s) in phosphosilicate which is the usual host in Er^{3+}/Yb^{3+} doped glass laser systems, rapid de-excitation to the laser upper level ${}^4I_{13/2}$ occurs, the probability of back transfer (k_{btr}) is markedly reduced due to this fast de-excitation and therefore is usually considered negligible. Thirdly, due to Er^{3+} - Er^{3+} cross relaxation, cooperative up-conversion (C_{up}) occurs, promoting an excited Er^{3+} ion from ${}^4I_{13/2}$ to level ${}^4I_{9/2}$. Also, interaction between a ground level Er^{3+} ion and two excited Yb^{3+} ion can create cumulative excitation of Er^{3+} ion to level ${}^4S_{3/2}$. However, since the population of level ${}^4I_{11/2}$ is very low, both cumulative energy transfer and back transfer from Er^{3+} to Yb^{3+} are considered negligible in the present work. Finally, excited Yb^{3+} ions (donors) transfer energy to nearby ground state Er^{3+} ions (acceptors), whereby the Er^{3+} becomes excited to the pump level ${}^4I_{11/2}$, while the Yb^{3+} drop to its ground state ${}^2F_{7/2}$.

Neglecting back-transfer, and only the ground state (${}^4I_{15/2}$, ${}^2F_{7/2}$) and the excited level (${}^4I_{13/2}$, ${}^2F_{5/2}$) of Er^{3+}/Yb^{3+} , the rate equations for the coupled Er^{3+}/Yb^{3+} can be written as [5-7]:

$$\frac{dn_2(r,z,t)}{dt} = W_{12} \cdot n_1(r,z,t) - W_{21} \cdot n_2(r,z,t) + k_{tr} n_4(r,z,t) \cdot n_1(z,t) - \frac{n_2(r,z,t)}{\tau_{er}} - C_{up} \cdot n_2^2(r,z,t) , \quad (1.1)$$

$$\frac{dn_4(r,z,t)}{dt} = R_{34}n_3(r,z,t) - R_{43}n_4(r,z,t) - \frac{n_4(r,z,t)}{\tau_{yb}} - k_{tr}n_4(r,z,t).n_1(r,z,t) , \quad (1.2)$$

$$n_{er} = n_1(r,z,t) + n_2(r,z,t) , \quad (1.3)$$

$$n_{yb} = n_3(r,z,t) + n_4(r,z,t) , \quad (1.4)$$

where W_{12} , W_{21} and τ_{yb} are the signal absorption rate, stimulated emission rate, and the spontaneous emission lifetime for Yb^{3+} ; R_{12} and R_{21} and τ_{er} are the pump absorption rate; stimulated emission rate, and spontaneous emission lifetime for Er^{3+} respectively; C_{up} is the upconversion coefficient. k_{tr} is the transfer coefficient from excited level Yb^{3+} to ground level Er^{3+} ; n_{er} and n_{yb} are the total ion concentrations of erbium and ytterbium; n_1 and n_2 are the ytterbium ion concentration in the ground state $^4\text{I}_{15/2}$ and the excited state $^4\text{I}_{13/2}$; n_3 and n_4 are the erbium ion concentration in the ground state $^2\text{I}_{7/2}$ and the excited state $^2\text{I}_{5/2}$ respectively.

For signal and pump absorption and stimulated emission rate, ignoring the amplified spontaneous emission (ASE), we have the following equations [8]:

$$W_{12}(r,z,t) = \frac{\sigma_{12}(v_s)P_s(z,t)\Gamma_s}{h\nu_s A} , \quad (1.5)$$

$$W_{21}(r,z,t) = \frac{\sigma_{21}(v_s)P_s(z,t)\Gamma_s}{h\nu_s A} , \quad (1.6)$$

and

$$R_{34} = \frac{\sigma_{34}(v_p)P_p(z,t)\Gamma_p}{h\nu_p A} , \quad (1.7)$$

$$R_{43} = \frac{\sigma_{43}(v_p)P_p(z,t)\Gamma_p}{h\nu_p A} , \quad (1.8)$$

where $\sigma_{12}(v_s)$ and $\sigma_{21}(v_s)$ are the absorption and stimulated emission cross sections of Yb^{3+} ions from the $^4\text{I}_{15/2}$ to the $^4\text{I}_{13/2}$ level; $\sigma_{34}(v_p)$ and $\sigma_{43}(v_p)$ are the

absorption and emission cross sections of Er^{3+} ions; Γ_p and Γ_s are the pump and signal overlap factor; A is the core area; P_p and P_s are the pump power and signal power respectively.

1.3 Numerical modeling of signal gain in Er-Yb fiber amplifier

In this section, I will first simplify the rate equations which describe the dynamics of Er-Yb fiber amplifiers. Then, incorporating the pump dissipation and signal gain equation, I solve the rate equations as the beams propagate in the fiber. With this information, one can determine the optimum fiber length, and the extractable power from the fiber amplifier.

1.3.1 Simplification of rate equations

At steady state, from Eq. (1.1)-(1.4), one can have:

$$W_{12}(n_{er} - n_2) - W_{21}n_2 + K_{tr}n_4(n_{er} - n_2) - \frac{n_2}{\tau_{er}} - C_{up}n_2^2 = 0 . \quad (1.9)$$

$$R_{34}(n_{yb} - n_4) - R_{43}n_4 - \frac{n_4}{\tau_{yb}} - K_{tr}n_4(n_{er} - n_2) = 0 . \quad (1.10)$$

From Eqs. (1.9) and (1.10), the ion concentration of the excited states n_2 , n_4 can be solved as function of W_{12} , W_{21} , R_{34} and R_{43} . Directly from Eq. (1.10), one can have:

$$n_4 = \frac{R_{34}n_{yb}}{R_{34} + R_{43} + \frac{1}{\tau_{yb}} + K_{tr}n_{er} - K_{tr}n_2} . \quad (1.11)$$

Insert the expression of n_4 into Eq. (1.9), and after simplifications, a cubic equation of n_2 can be obtained as:

$$\begin{aligned}
& C_{up} K_{tr} n_2^3 + \left[\left(W_{12} + W_{21} + \frac{1}{\tau_{er}} \right) K_{tr} - \left(R_{34} + R_{43} + \frac{1}{\tau_{yb}} + K_{tr} n_{er} \right) C_{up} \right] n_2^2 \\
& + \left[-W_{12} K_{tr} n_{er} - \left(W_{12} + W_{21} + \frac{1}{\tau_{er}} \right) \left(R_{34} + R_{43} + \frac{1}{\tau_{yb}} + K_{tr} n_{er} \right) - K_{tr} R_{34} n_{yb} \right] n_2 \\
& + \left[W_{12} n_{er} \left(R_{34} + R_{43} + \frac{1}{\tau_{yb}} + K_{tr} n_{er} \right) + K_{tr} R_{34} n_{yb} n_{er} \right] = 0 .
\end{aligned} \tag{1.12}$$

This cubic equation has 3 roots for n_2 that can be solved with a standard method.

It is found that only one root is physically allowed. With Eqs. (1.5)-(1.8), equation (1.11), and (1.12) can be written as:

$$n_4 = \frac{P_P(z) n_{yb} C_1}{P_P(z) C_2 + \frac{1}{\tau_{yb}} + K_{tr} n_{er} - K_{tr} n_2} , \tag{1.13}$$

and

$$\begin{aligned}
& n_2^3 + \left[-n_{er} + \frac{\left(\frac{1}{\tau_{er}} + W_{12}(z) + W_{21}(z) \right) \left(P_P(z) C_2 + \frac{1}{\tau_{yb}} \right)}{C_{up} K_{tr}} \right] n_2^2 \\
& - \left(\frac{n_{er}}{C_{up} \tau_{er}} + \frac{2n_{er} W_{12}(z)}{C_{up}} + \frac{n_{er} W_{21}(z)}{C_{up}} + \frac{C_1 P_P(z)}{C_{up}} \right. \\
& \left. + \frac{\left(P_P(z) C_2 + \frac{1}{\tau_{yb}} \right) \left(\frac{1}{\tau_{er}} + W_{12}(z) + W_{21}(z) \right)}{C_{up} K_{tr}} \right) n + \\
& \frac{C_1 n_{er} P_P(z)}{C_{up}} + \frac{W_{12}(z) n_{er}^2}{C_{up}} + \frac{W_{12}(z) n_{er} \left(P_P(z) C_2 + \frac{1}{\tau_{yb}} \right)}{C_{up} K_{tr}} = 0
\end{aligned} \tag{1.14}$$

where C_1 and C_2 are:

$$C_1 = \frac{\Gamma_P \sigma_{34}(v_P) n_{er}}{h v_P A}, \quad (1.15)$$

and

$$C_2 = \frac{\Gamma_P (\sigma_{34}(v_P) + \sigma_{43}(v_P))}{h v_P A}, \quad (1.16)$$

For a cubic equation that is in the form of

$$x^3 + ax^2 + bx + c = 0. \quad (1.17)$$

The solution that is physically allowed for Eq. (1.14) takes the form of

$$x = -\frac{a}{3} - (0.5 + 0.5\sqrt{3}i)^3 \sqrt[3]{-\frac{q}{2} + \sqrt{\frac{q^2}{4} + \frac{p^3}{27}}} + (-0.5 + 0.5\sqrt{3}i)^3 \sqrt[3]{-\frac{q}{2} - \sqrt{\frac{q^2}{4} + \frac{p^3}{27}}}, \quad (1.18)$$

where

$$p = b - \frac{a^2}{3}, \quad (1.19)$$

$$q = c + \frac{2a^3 - 9ab}{27}. \quad (1.20)$$

after n_2 is solved, n_4 can be find from Eq. (1.13). Then from Eqs. (1.3) and (1.4), the ground state and excited state population densities of erbium and ytterbium can easily be computed.

1.3.2 Pump dissipation and signal gain simulation

The pump dissipation and signal gain as function of propagation distance z are numerically simulated here. Ignoring excess losses, the pump dissipation is governed by the differential equation as [8]:

$$\frac{dP_P(z)}{dz} = \Gamma_P(\sigma_{43}(v_P)n_4(z) - \sigma_{34}(v_P)n_3(z))P_P(z) \quad , \quad (1.21)$$

and the signal gain is governed by the differential equation as:

$$\frac{dP_S(z)}{dz} = \Gamma_S(\sigma_{21}(v_S)n_2(z) - \sigma_{12}(v_S)n_1(z))P_S(z) \quad . \quad (1.22)$$

Eqs. (1.3), (1.4), (1.13), (1.14), (1.21) and (1.22) can be combined together to solve the pump dissipation and signal gain. The parameters used in this simulation are listed in Table 1-1 [5, 8].

Symbol	Value
n_{er}	$7.1 \times 10^{26} \text{ m}^{-3}$
n_{yb}	$0.9 \times 10^{27} \text{ m}^{-3}$
τ_{yb}	$1.5 \times 10^{-3} \text{ s}$
τ_{er}	$1.1 \times 10^{-2} \text{ s}$
k_{fr}	$5.0 \times 10^{-22} \text{ m}^3/\text{s}$
C_{up}	$1.0 \times 10^{-24} \text{ m}^3/\text{s}$
A	$1.52 \times 10^{-11} \text{ m}^2$
σ_{43}	$4.9 \times 10^{-25} \text{ m}^2$
σ_{34}	$2.1 \times 10^{-25} \text{ m}^2$
λ_P	990 nm
λ_S	1.54 μm
σ_{12}	$5.63 \times 10^{-25} \text{ m}^2$
σ_{21}	$5.75 \times 10^{-25} \text{ m}^2$
Γ_P	0.7
Γ_S	0.27

Table 1-1. Parameters of the Er/Yb amplifier

The flow chart for the simulation of signal gain and pump dissipation as the signal and pump propagate in the fiber is shown in Figure 1-2.

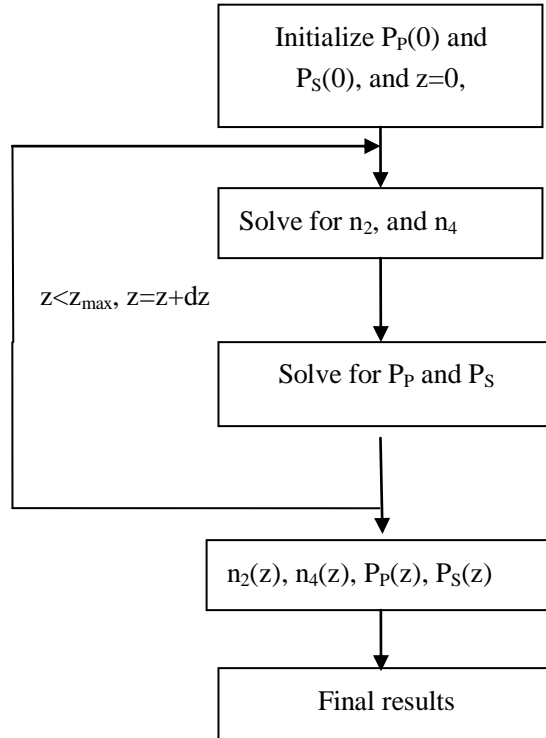


Figure 1-2. Flow chart of the signal gain and pump dissipation calculation.

Initially the pump power is set at 0.1 W, and the signal at 10 nW for the simulation. The upper level ion concentrations of ytterbium and erbium are shown in Figure 1-3 and 1-4. And it can be seen that initially the upper-level populations remain constant which means the pump is still very strong. Then the upper-level populations drop due to the stimulated emission of photons. The pump dissipation is shown in Figure 1-5. It can be seen that the pump power decreases exponentially. The point where the pump remains about 3% is used to determine the optimum fiber length. From Figure 1-6, it can be seen that the signal increases, and reaches the maximum at the optimum fiber length, after which the signal power drops owing to the absorption of the signal by the fiber itself. In Figure 1-7, the signal gain is plotted in dB. This plot again shows the

importance of optimum fiber length.

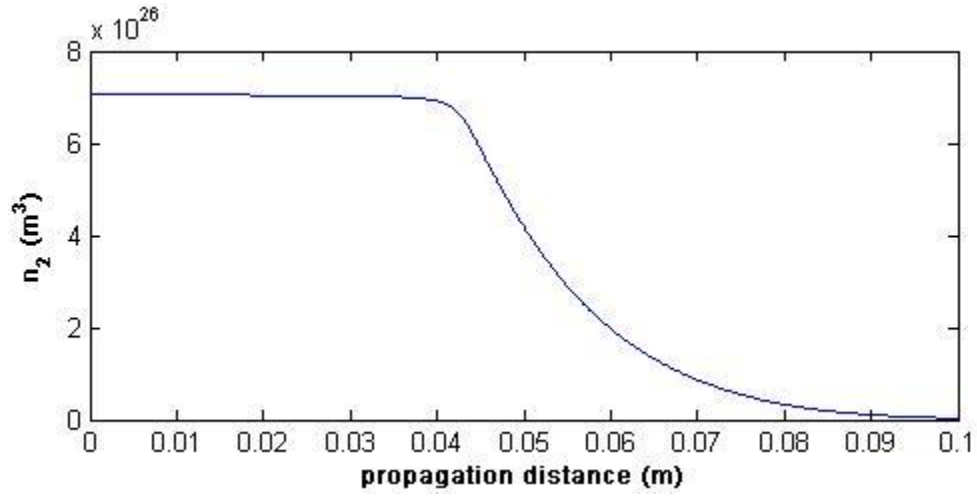


Figure 1-3. Upper-level population concentration of Erbium.

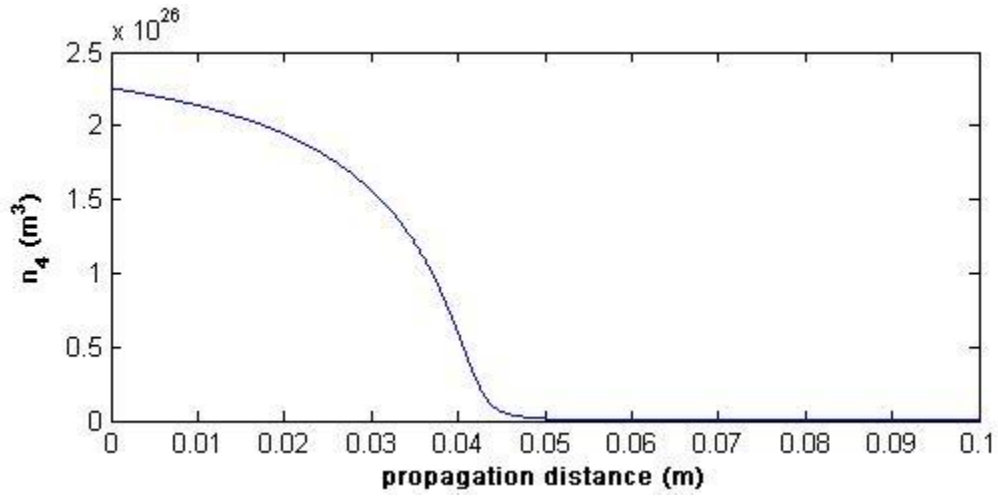


Figure 1-4. Upper-level population concentration of Ytterbium.

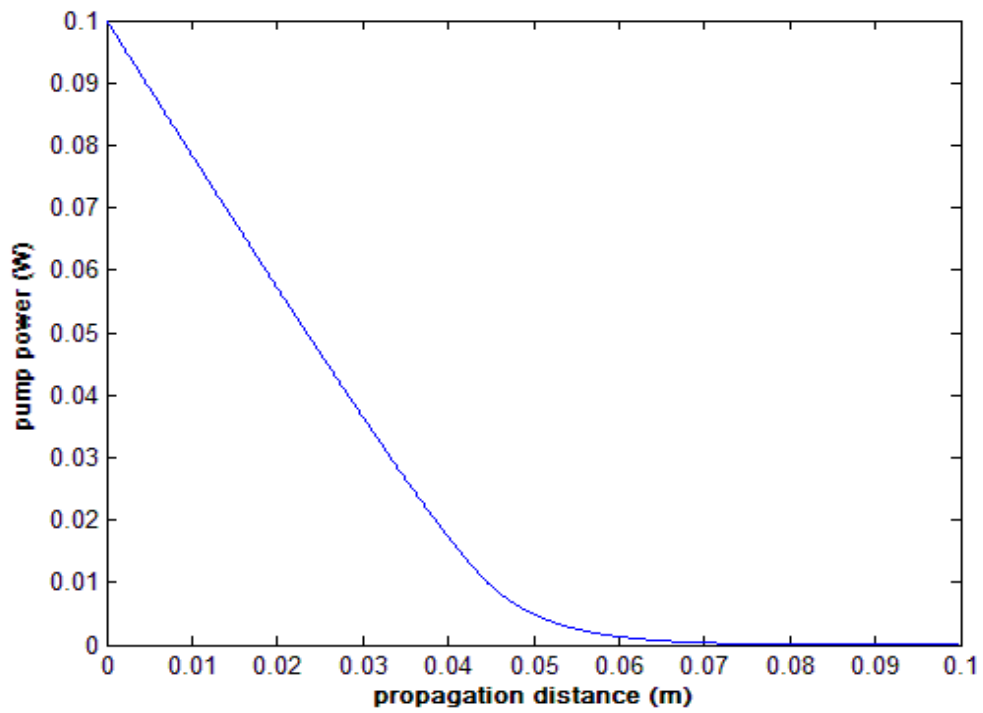


Figure 1-5. Pump power dissipation vs. propagation distance.

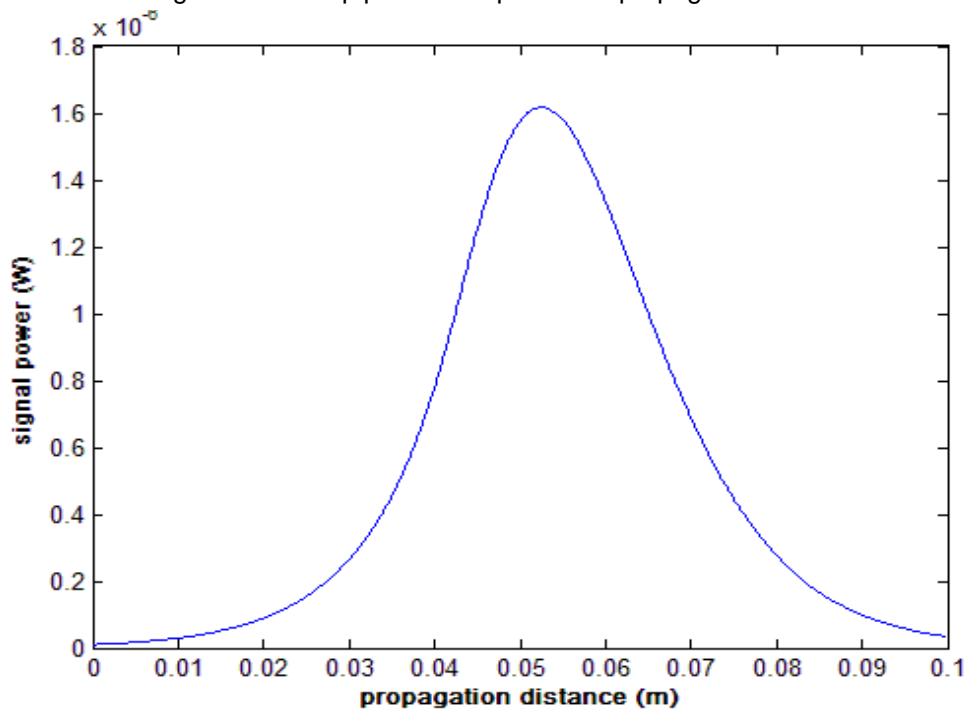


Figure 1-6. Signal power vs. propagation distance.

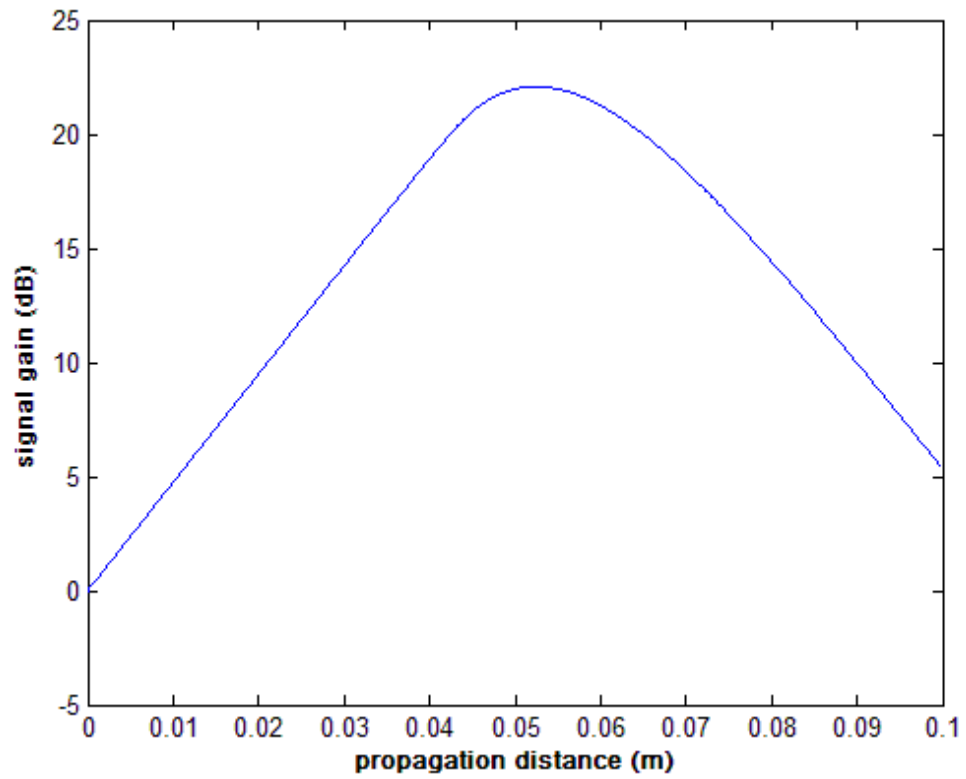


Figure 1-7. Signal gain in dB vs. propagation distance.

1.4 Summary

In this chapter an erbium-ytterbium co-doped fiber amplifier system is introduced. I studied the dynamics of this type of fiber amplifier and simulated the signal gain and pump dissipation in the fiber system. The simulation results can be used to determine how various factors such as dopants concentration, fiber core size, fiber length etc would affect the gain in the fiber. The simulation results serve as a guide for further development of high power fiber lasers with wavelength tunability.

CHAPTER II

MODELING OF BEAM PROPAGATION IN GAIN-GUIDED FIBER

In this Chapter, I theoretically examine self-focusing, and self-phase modulation effects in gain-guided (GG) optical fibers. The effects are investigated by propagating a spatial-temporal pulse in GG fibers. By looking at the pulse at different distances in the fiber, those effects are analyzed. After propagation in the GG fiber, the pulse is coupled into a standard single mode fiber (SMF). The power transmission characteristics and the dispersion in the single mode fiber are investigated.

2.1 Introduction to gain-guided fiber

Gain-guiding effects have been discussed for more than forty years. In 1965, Kogelnik analyzed the wave propagation in media with gain variations [9]. Later on, experiments with semiconductor lasers demonstrated gain-guiding in laser resonators [10]. At the same time, media with different gain profiles have been investigated both in literature and experiments [11-13]. In 2003, Siegman proposed a complete description of gain-guiding in slab-waveguide, and optical

fibers [14]. Lasing in gain-guided, index anti-guided (GG+IAG) fiber has been demonstrated recently by several researchers [15-17]. Lasing in GG+IAG fibers possess a transverse profile with single mode characteristics. Thus, fiber with gain and an extremely large core radius is a good candidate in developing of high power fiber lasers. With fiber lasers in mind, recent papers have studied gain-saturation effects in slab wave guided and optical fibers [18, 19]. In this Chapter, GG+IAG fiber with self-phase modulation is studied for self-focusing.

Large mode area (LMA) fibers can suppress nonlinear effects such as Stimulated Brillouin Scattering (SBS) or Stimulated Raman Scattering (SRS) [20, 21] while still exhibiting single mode output and this is desired for many applications. Fiber designs have been proposed to achieve single transverse mode lasing. For instance, the multi-core fiber with phase-locked modes has been demonstrated [22]. Also, exploiting index-matched core-cladding fiber designs has been shown to improve higher-order mode suppression in solid or microstructured fibers [23].

2.2 Theoretical analysis

The propagating modes in gain-guided fiber are described in section 2.2.1. In section 2.2.2, I present the spatial-temporal pulse propagation equation governed by Nonlinear Schrödinger equation (NLSE) in the GG fiber. The nonlinear refractive index effects the pulse propagation and will lead to self-focusing and self-phase modulation in GG fibers. In section 2.2.3 we present the numerical algorithm for solving the NLSE.

2.2.1 Modes in gain-guided fiber

In traditional step index-guided fibers, the modes are described by Bessel's functions of the first and second kind in the core and cladding respectively. The mathematical description of the fiber modes in GG fibers are analogous, except the V number is replaced with complex \tilde{V} number by Siegman [24], where the imaginary part comes from the contribution of the gain in the core. The real part is the conventional V number, and its square is given as:

$$V^2 = \Delta N = 2n_o \left(\frac{2\pi a}{\lambda} \right)^2 \Delta n , \quad (2.1)$$

where a is the core radius, Δn is the index contrast of the core and the cladding region, n_o is the average index of the core-cladding materials, and λ is the signal wavelength. The complex \tilde{V} number is obtained by:

$$\tilde{V}^2 = \Delta N + iG . \quad (2.2)$$

The imaginary part of the complex \tilde{V} number is defined as:

$$G = \frac{n_o \lambda}{2\pi} \left(\frac{2\pi a}{\lambda} \right)^2 g , \quad (2.3)$$

where g is the power gain coefficient in the core. If $\Delta n > 0$ and $g = 0$, the fiber corresponds to the usual guided fiber geometry, and if $\Delta n < 0$ and $g > 0$, the fiber is called GG+IAG fiber.

The field profile for LP₀₁ and LP₁₁ mode are given as:

$$E_{0l}(r) = \begin{cases} J_l\left(\frac{\tilde{u}r}{a}\right), & r \leq a \\ \frac{J_l(\tilde{u})K_l\left(\frac{\tilde{w}r}{a}\right)}{\tilde{w}K_l(\tilde{w})}, & r > a \end{cases} , \quad (2.4)$$

where $l = 0$ and $l = 1$ correspond to the LP₀₁ and LP₁₁ mode respectively. \tilde{u} and \tilde{w} are related by the propagation equation:

$$\tilde{u}^2 + \tilde{w}^2 = \tilde{V}^2 . \quad (2.5)$$

Since \tilde{V} is a complex number, \tilde{u} and \tilde{w} both are also complex numbers, so \tilde{w} can be written as:

$$\tilde{w} = w_r + jw_i . \quad (2.6)$$

By using the continuity of the field at the cladding/core interface, \tilde{u} and \tilde{w} can be approximated as:

$$w_r \cong \left(\frac{j_{0l}}{-\Delta N} \right) \times \left[\frac{G}{G_{th}} - 1 \right] , \quad (2.7)$$

$$w_i \cong \sqrt{-\Delta N} , \quad (2.8)$$

and

$$\tilde{u} \cong j_{0l}(\tilde{w} - 1)/\tilde{w} . \quad (2.9)$$

For LP₀₁ mode, $l=0$, $G_{th} \cong \sqrt{\frac{133.8}{-\Delta N}}$; for LP₁₁, $l=1$, and $G_{th} \cong \sqrt{\frac{862.2}{-\Delta N}}$. $j_{01} \cong 2.405$, and $j_{11} \cong 3.8317$ are the cut off value of Bessel function, and they correspond to LP₀₁ and LP₁₁ mode respectively.

2.2.2 Nonlinear Schrödinger equation (NLSE)

The spatial-temporal pulse propagation in the fiber is determined by the NLSE. Assuming a slowly varying amplitude $A(x, y, z, \tau)$, and using the paraxial approximation, NLSE can be written as:

$$\frac{\partial A(x,y,z,\tau)}{\partial z} = \frac{i}{2k} \nabla_{\perp}^2 A(x, y, z, \tau) + \frac{i}{2k} \left(\frac{\omega}{c}\right)^2 (n_{co}^2 - n_{cl}^2) A(x, y, z, \tau) - i \frac{\beta_2}{2} \frac{\partial^2 A}{\partial \tau^2} + i\gamma |A(x, y, z, \tau)|^2 A(x, y, z, \tau) - \frac{\alpha}{2} A(x, y, z, \tau), \quad (2.10)$$

where ∇_{\perp}^2 is the 2-D Laplacian operator which describes the diffraction. In cylindrical coordinate, we have $r^2 = x^2 + y^2$, so the operator becomes:

$$\nabla_{\perp}^2 = \frac{\partial^2}{\partial r^2} + \frac{1}{r} \frac{\partial}{\partial r}, \quad (2.11)$$

n_{co} is the core index, including the gain induced index n_i , it is written as:

$$n_{co} = n_r + in_i, \quad (2.12)$$

where $n_i = -\left(\frac{g}{2k_0}\right)$, g is the power gain coefficient, $k_0 = 2\pi/\lambda_{vac}$ is the wave number in vacuum, where λ_{vac} is the central wavelength of the pulse in vacuum. k is the wave number in the cladding of the fiber which is given by $\left(\frac{\omega}{c}\right)n_{cl}$, where ω is the central frequency of the pulse, c is the velocity of light, n_{cl} is the cladding refractive index. It can also include gain or loss terms as its imaginary part. β_2 is

the group velocity dispersion parameter; in silica glass it is $-26 \text{ fs}^2/\text{mm}$ and in single mode fiber it is $-20 \text{ fs}^2/\text{mm}$ [25]. The nonlinearity coefficient $\gamma = k_0 n_2$, where n_2 is the nonlinear index in silica, which is $3.0 \times 10^{-8} \text{ } \mu\text{m}^2/\text{Watt}$ [25, 26], and α is an absorption coefficient which is assumed to be negligible in our simulations.

2.2.3 Numerical algorithm solving pulse propagation

Since the fiber is circularly symmetric; assuming a cylindrical symmetry for the pulse amplitude, i.e. $A(x, y, z, \tau) \rightarrow A(r, z, \tau)$, is suitable and will simplify the simulation. In the transverse direction, we apply a 1-D Hankel transform instead of a 2-D Fourier transform, making the numerical simulations run much faster and saving computational memory. In the time domain, a 1-D Fourier transform is applied. In order to solve Eq. (10), we write the equation with operators:

$$\frac{\partial A(z)}{\partial z} = \mathcal{L}_r A(z) + \mathcal{L}_D A(z) + \mathcal{L}_I A(z) + \mathcal{N}(A(z)) \cdot A(z), \quad (2.13)$$

where $\mathcal{L}_r = \frac{i}{2k} \Delta_{\perp}^2$ is the diffraction operator, $\mathcal{L}_D = -i \frac{\beta_2}{2} \frac{\partial^2}{\partial \tau^2}$ is the dispersion term, $\mathcal{L}_I = \frac{i}{2k} \left(\frac{\omega}{c}\right)^2 (n_{co}^2 - n_{cl}^2)$ is the complex index term, which includes gain guiding in the core, and $\mathcal{N}(A(z)) = i\gamma |A(z)|^2$ is the nonlinear self-phase modulation term.

By solving Eq. (2.13), the field at $z + \Delta z$ is obtained:

$$A(z + \Delta z) = Z\{e^{\int_z^{z+\Delta z} (\mathcal{L}_r + \mathcal{L}_D + \mathcal{N}(A(z)) + \mathcal{L}_I) dz}\} A(z), \quad (2.14)$$

where $Z\{\dots\}$ is the normal order of operators with respect to z . Eq. (2.14) can be approximately written as:

$$A(z + \Delta z) = e^{(\mathcal{L}_r + \mathcal{L}_D)\frac{\Delta z}{2}} \cdot e^{\mathcal{L}_I \Delta z} \cdot e^{\mathcal{N}(A)\Delta z} \cdot e^{(\mathcal{L}_r + \mathcal{L}_D)\frac{\Delta z}{2}} A(z) . \quad (2.15)$$

Write Eq. (2.14) in the split-step method form:

$$A(z + \Delta z) = e^{\mathcal{L}_r \frac{\Delta z}{2}} e^{\mathcal{L}_D \frac{\Delta z}{2}} \cdot e^{\mathcal{L}_I \Delta z} \cdot e^{\mathcal{N}(A)\Delta z} \cdot e^{\mathcal{L}_r \frac{\Delta z}{2}} e^{\mathcal{L}_D \frac{\Delta z}{2}} A(z) . \quad (2.16)$$

This form is the second approximation to Eq. (2.13), thus give more accuracy for the numerical simulation. In the following part, the action of each operator in Eq. (2.16) is described from the right the left for the operator actions.

The pulse propagation under temporal dispersion can be described as:

$$A(\tau, z + \frac{\Delta z}{2}) = e^{\mathcal{L}_D \frac{\Delta z}{2}} A(\tau, z) = e^{-i\frac{\beta_2}{2} \frac{\partial^2}{\partial \tau^2} \cdot (\frac{\Delta z}{2})} A(\tau, z) . \quad (2.17)$$

Eq. (2.17) is solved by using a 1-D fast Fourier transform (FFT) with respect to τ .

Use Fourier transform property of derivatives, we have:

$$\frac{\partial^2 A(\tau, z)}{\partial \tau^2} \xrightarrow{FFT} -\omega^2 FFT(A(\tau, z)) , \quad (2.18)$$

where ω denotes the temporal angular frequency in the Fourier space. Thus, the solution of Eq. (2.18) is:

$$A\left(\tau, z + \frac{\Delta z}{2}\right) = FFT^{-1} \left\{ e^{-i\frac{(-\beta_2)\omega^2}{4}\Delta z} FFT\{A(\tau, z)\} \right\} , \quad (2.19)$$

For propagation with diffraction, we apply the Fast Hankel Transform (FHT).

Write 2-D Laplacian operator in the cylindrical coordinate as described in Eq.

(2.11), the propagation equation can be written as:

$$A\left(r, z + \frac{\Delta z}{2}\right) = e^{\mathcal{L}_r \frac{\Delta z}{2}} A(r, z) = e^{\frac{i}{2k} \left(\frac{\partial^2}{\partial r^2} + \frac{1}{r} \frac{\partial}{\partial r} \right) \cdot (\frac{\Delta z}{2})} A(r, z) . \quad (2.20)$$

The FHT of the Laplacian operator with respect to r is:

$$\frac{i}{2k} \left(\frac{\partial^2}{\partial r^2} + \frac{1}{r} \frac{\partial}{\partial r} \right) A(r, z) \xrightarrow{FHT} -\frac{i}{2k} 4\pi^2 \rho^2 FHT\{A(r, z)\} . \quad (2.21)$$

Thus, Eq. (2.20) is expressed as [27]:

$$A\left(r, z + \frac{\Delta z}{2}\right) = FHT^{-1}\left\{\exp\left[-i\frac{\pi^2}{k}\rho^2\Delta z\right] \cdot A_{\mathcal{H}}(\rho, t)\right\}, \quad (2.22)$$

where $A_{\mathcal{H}}(\rho, z)$ is $FHT\{A(r, z)\}$, the Hankel transform of $A(r, z)$ with respect to r , and the Hankel transform $A_{\mathcal{H}}(\rho, t)$ is defines as:

$$A_{\mathcal{H}}(\rho, z) = 2\pi \int_0^\infty A(r, z) J_0(\rho \cdot r) dr, \quad (2.23)$$

where $J_0(\dots)$ denote the zero-order of Bessel function of the first kind. Also, note that the forward and inverse Hankel transform take the same form as Eq. (2.23), and the quasi-discrete Hankel transform is used to evaluate the zero-order transform [28, 29].

The propagation with gain guiding is described as:

$$A(z + \Delta z) = \exp\left[\frac{i}{2k}\left(\frac{\omega}{c}\right)^2 (n_{co}^2 - n_{cl}^2)\Delta z\right] \cdot A(z). \quad (2.24)$$

With nonlinear index, the field at $z + \Delta z$ is:

$$A(z + \Delta z) = \exp\left[i\gamma \cdot |A(z)|^2 \cdot \Delta z\right] \cdot A(z). \quad (2.25)$$

The pulse propagation under dispersion and diffraction needs another $\Delta z/2$ propagation in order to find the field at $z + \Delta z$. For the remaining $\Delta z/2$ step, we use the start field obtained through the calculation above, and the process of solving the field is the same as Eqs. (2.16-2.25). By repeating all the processes described from Eqs. (2.16-2.25), one can propagate the beam for a desired distance in the fiber.

In summary, the NLSE is solved by incorporating the Fast Hankel

Transform and The Fast Fourier transform method. There are also many other numerical methods for solving the NLSE. For example, for non-cylindrical symmetric pulse or waveguide, one can use 2D FFT in for the transverse spatial direction. Also, the Crank-Nicolson algorithm combined with transparent boundary condition can be applied to solve the pulse propagation in the transverse spatial direction [30, 31]. Those methods have been used for checking our FHT algorithm.

2.3 Simulation results

The GG fiber used in the simulation has core index 1.579, and cladding index 1.5689, they are taken from Ref. [15], (we notice that index-guiding or anti-index guiding doesn't change our simulation results at all), the gain we chose is $g = 0.7\text{cm}^{-1}$, and the nonlinear refractive index is $3.0 \times 10^{-8} \mu\text{m}^2/\text{Watt}$ [25, 26], and the signal wavelength is $1.55 \mu\text{m}$. We use three different core radii which are $50 \mu\text{m}$, $75 \mu\text{m}$, and $100 \mu\text{m}$ respectively for the GG fiber. The input pulse to the GG fiber is defined as a Gaussian function in space and time:

$$A(r, t, z = 0) = A_0 e^{-(1+j \cdot P_{curve}) \cdot r^2 / 2w_0^2} \cdot e^{-t^2 / 2\tau^2}, \quad (2.26)$$

where A_0 is the initial field amplitude which has units of $2.0 W^{1/2} \cdot \mu\text{m}^{-1}$, w_0 is the transverse pulse width which is taken as $50 \mu\text{m}$, and $\tau = 1\text{ps}$ is the pulse width, and the initial temporal phase curvature is $P_{curve} = 0$, which means the initial pulse is not chirped. With enough initial pulse energy, the pulse will begin focusing after propagating about 10 centimeters. The numerical simulation stops before the pulse completely collapses, since our numerical technique cannot capture the high frequencies introduced by further collapse. At the end of the GG fiber the pulse is coupled into a standard single mode fiber, where we study the power transmission and the phase of the pulse.

2.3.1 Self-focusing and collapsing in GG fiber

The pulse propagation is simulated in GG fiber with three different core

radii which are 50 μm , 75 μm , and 100 μm respectively. Figure 2-1(a) is the initial pulse at the input of the GG fiber. Figures 2(b)-(d) show pulse propagation in the 50 μm core radius of the fiber at positions 10 cm, 11 cm and 11.2 from the input, resp. Figures 2(e)-(g) are three snapshots for pulse propagation in the 75 μm core radius fiber at are 8.4 cm, 9.0 cm, and 9.2cm, resp. Figures 8(h)-(j) are for the pulse propagation in the 100 μm core radius fiber at 8.2 cm, 8.8 cm, and 9.0 cm, resp. These figures have confirmed self-focusing, and collapsing of the pulses in the GG fibers. For different core size the distance the pulses need to propagate to start self-focusing and collapsing are different. For smaller core size the distance is bigger, this is because the critical power to collapse [32] is almost a constant parameter for different core sizes, however, for smaller core sizes the transverse gain is smaller, therefore the pulse must propagate a greater distance.

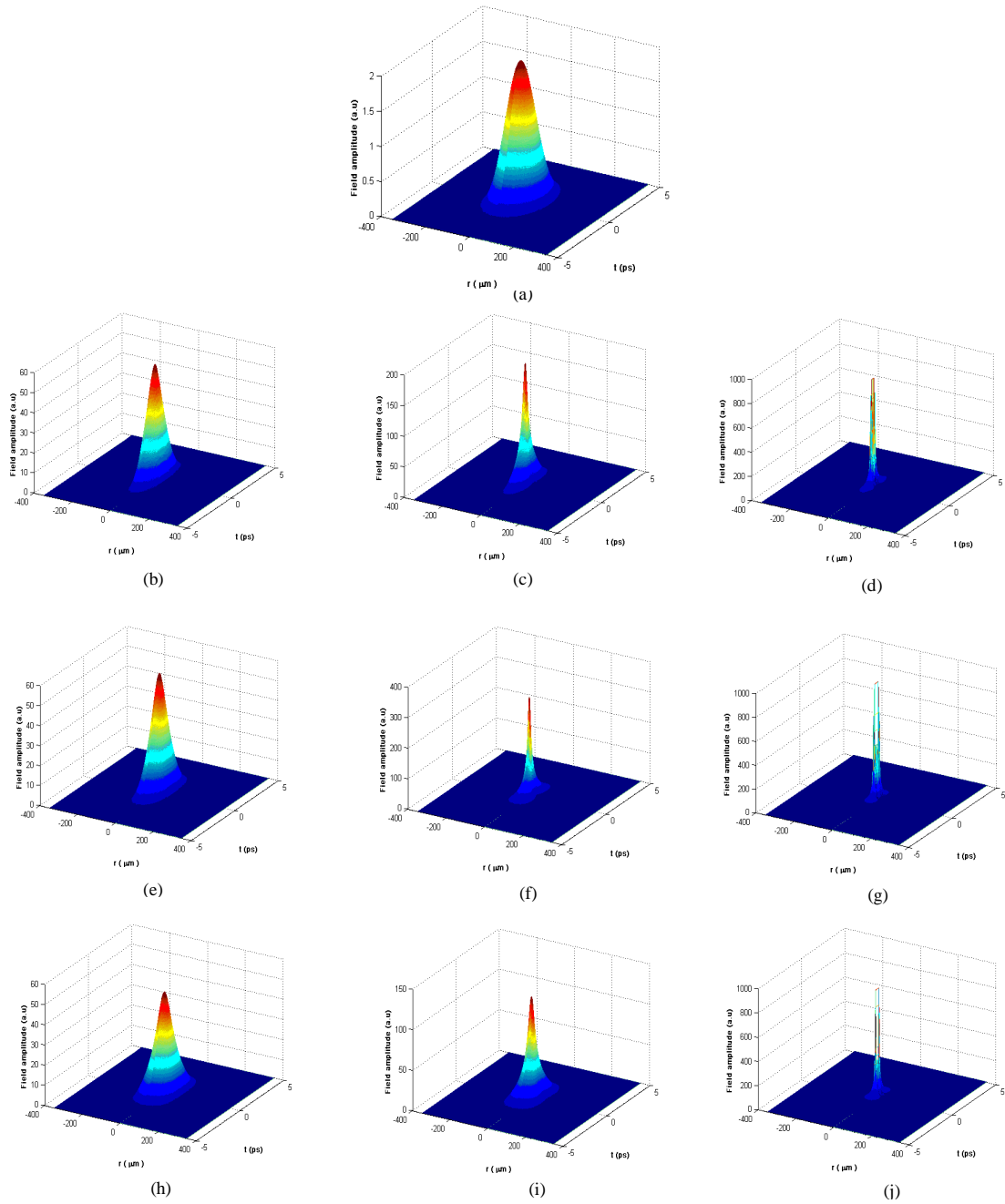


Figure 2-1. Field amplitudes of the spatial-temporal pulse propagations in GG fiber. (a) is the initial pulse; (b)-(d) correspond to the pulse propagation in the 50 μm core radius of the fiber, and the distances are 10 cm, 11 cm, 11.2cm, respectively; (e)-(g) correspond to the pulse propagation in the 75 μm core radius of the fiber, and the distances are 8.4 cm, 9.0 cm, 9.2cm, respectively; (h)-(j) correspond to the pulse propagation in the 100 μm core radius of the fiber, and the distances are 8.2 cm, 8.8 cm, 9.0cm, respectively.

2.3.2 Self-phase modulation In GG fiber

For this section, the on-axis ($r=0$) phase for the pulse propagating in the GG fiber is investigated. Figure 2-2 displays the on-axis phase evolutions as the pulses propagate in three fibers with three different core radii. Figure 2-2(a) is the on-axis phase of the initial start pulse. It is a flat phase without any curvature. Figures 2-2(b)-(d), (e)-(g), and (h)-(j) are the on-axis phase evolutions for 50 μm , 75 μm , and 100 μm core radii, respectively. The locations are chosen as the same in Figures 2-1. In the figures, it shown as the pulse start to focus quickly in space, it will develop a phase curvature in time equivalently. For the 50 μm core radius, the phase is higher than other cases, this is because the pulse has propagated more distance in this fiber, thus has accumulated more phase contrast.

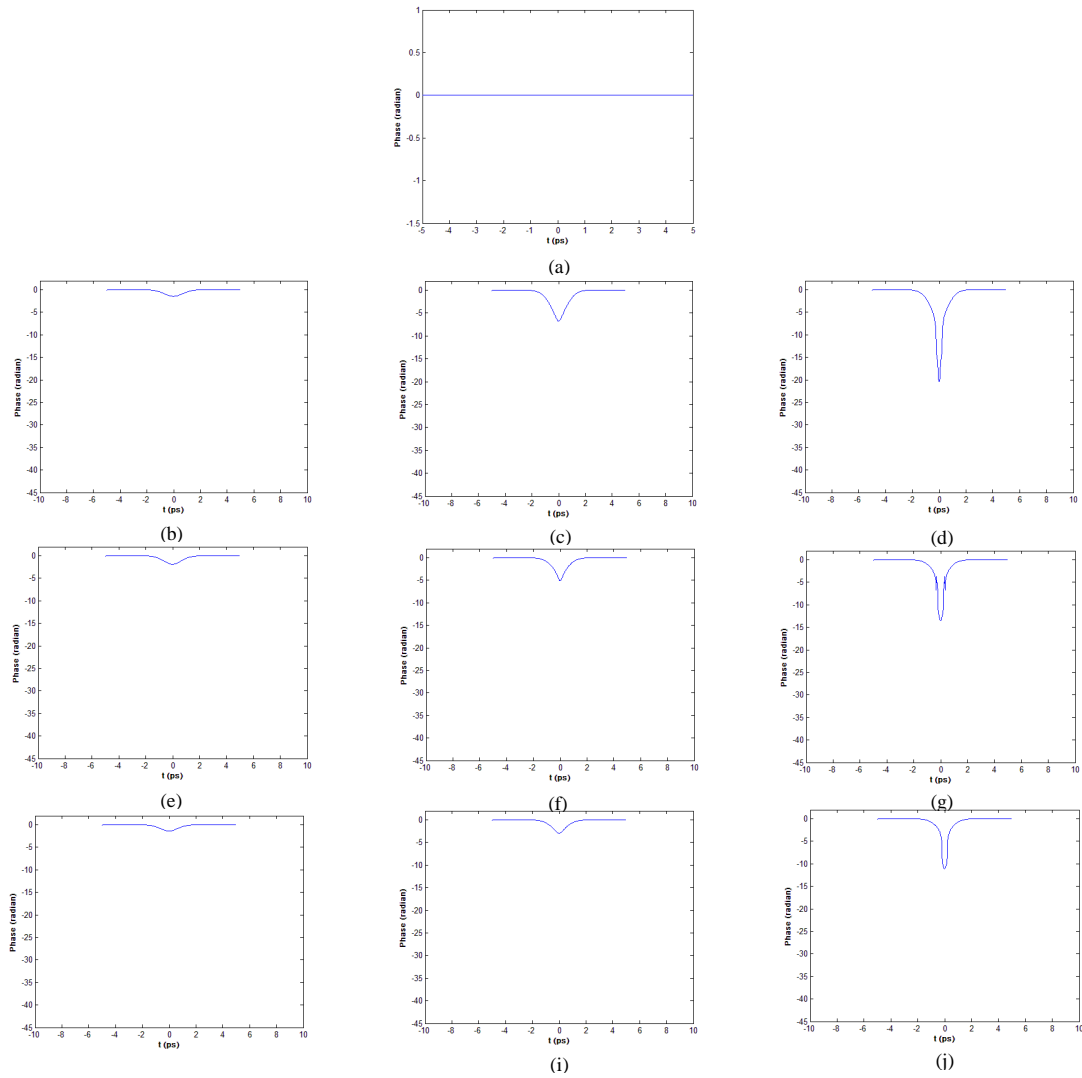


Figure 2-2. On-axis phase evolution for the pulses propagation in the GG fiber. (a) is the phase for the initial pulse; (b)-(d) are the phases corresponding to pulse propagation in the 50 μm core radius of the fiber, and the distances are 10 cm, 11 cm, 11.2cm, respectively; (e)-(g) are the phases corresponding to pulse propagation in the 75 μm core radius of the fiber, and the distances are 8.4 cm, 9.0 cm, 9.2cm, respectively; (h)-(j) are the phases corresponding to pulse propagation in the 100 μm core radius of the fiber, and the distances are 8.2 cm, 8.8 cm, 9.0cm, respectively.

2.3.3 Pulse coupling into single mode fiber

The pulses are coupled into a standard single mode fiber with 4.5 μm core radius at the end of the GG fiber span; see the illustration in Figure 2-3. The

Gaussian width of the single mode fiber is calculated through Eq. (2.26) [25]:

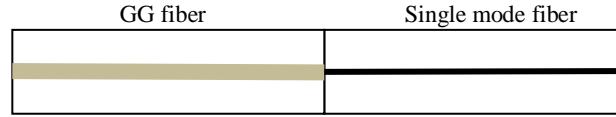


Figure 2-3. GG fiber is spliced to a single mode fiber.

$$w \approx a \left(0.65 + 1.619V^{-\frac{3}{2}} + 2.879V^{-6} \right) , \quad (2.27)$$

where a is the core radius of the single mode fiber, the V number is taken as 2.4 in the simulation. Thus, the width is found to be $4.95 \mu\text{m}$. The field and power coupling is calculated through Ref [33]. The phase and amplitude of the pulse are extracted after the field is coupled into the fiber. The power in the GG fiber and single-mode fiber is calculated by integrating the field intensity over the transverse direction at each time point. Multiply the field at the end of the GG fiber at each time point with the corresponding single-mode fiber mode profile, the power and phase transmitted into the single mode fiber is obtained. The power transmission is defined as the transmission from the start of the GG fiber to the single mode fiber, since we are interested how the pulse input in the GG fiber would affect the pulses in the single mode fiber. Figures 2-4(a), (c), (e), are the transmitted power for the single-mode fiber as a function of the input to the GG fiber. From the results, we found at lower input power, the slope efficiency is small and stable, which indicates the coupling efficiency from GG fiber to single mode fiber is inefficient. The reason is at smaller input power, the GG fiber mode

beam width is much wider than the single-mode fiber mode profile. As the input power into the GG fiber increases, the pulse will focus at the end of the GG fiber and the overlap between the field profile in GG fiber and single mode fiber profile improves, thus giving rise to a higher coupling efficiency. However, as the input power continues to increase, the pulse at the end of the GG fiber continues to collapse which will lead to a precipitous drop in the coupling efficiency, which is due to a mode mismatch between the GG fiber and the SM fiber. The coupling efficiency becomes erratic near the critical collapse power and results are not followed beyond this point. Figure 2-4(b), (d), (f) are the phases in the single mode fiber versus the input power. The phase curves follow the transmission curves. The phase contrast is bigger for the 50 μm GG fiber core radius than for the other core radii, this is the same as Figure 2-2, because the pulse propagated a longer distance in the GG fiber and accumulated a bigger phase contrast.

These results are used to infer the spread of the pulse in the single mode fiber. A phase change of 12 radians from the pulse center to the 1/e intensity point corresponds to a chirp parameter, $C \left(\phi(t) = \frac{C}{2} \left(\frac{t}{T_0} \right)^2 \right)$ of 24. The fiber length for dispersion compensation for shorter pulses is reduced and the compensation fiber could be inserted in a fiber laser cavity to balance the dispersion in each round trip.

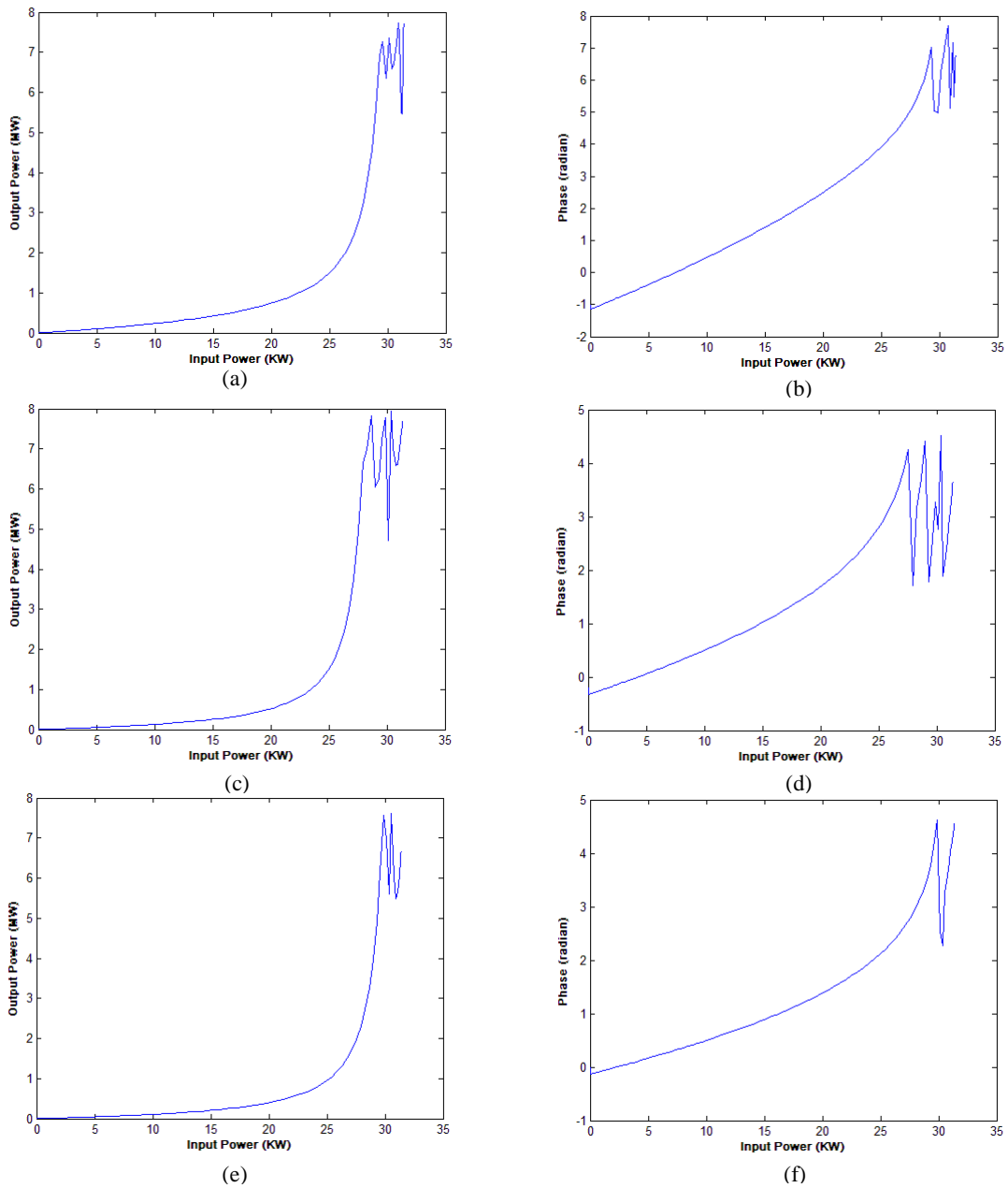


Figure 2-4. Power in the single mode fiber versus input power coupled into the GG fiber. (a), (c), and (e) are power the transmission curves for 50 μm , 75 μm , and 100 μm core size respectively, and the GG fiber lengths are 11.2 cm, 9.2 cm, and 9.0 cm accordingly. (b), (d), and (f) are the phase curves for 50 μm , 75 μm , and 100 μm core size respectively.

2.4 Kerr-lens mode-locking with gain-guided fiber

Kerr-lens mode-locking (KLM) can be used to generate short pulse with high peak power. To achieve KLM, self-focusing which requires high enough power is necessary, thus KLM operate at the pulse power close to critical power.

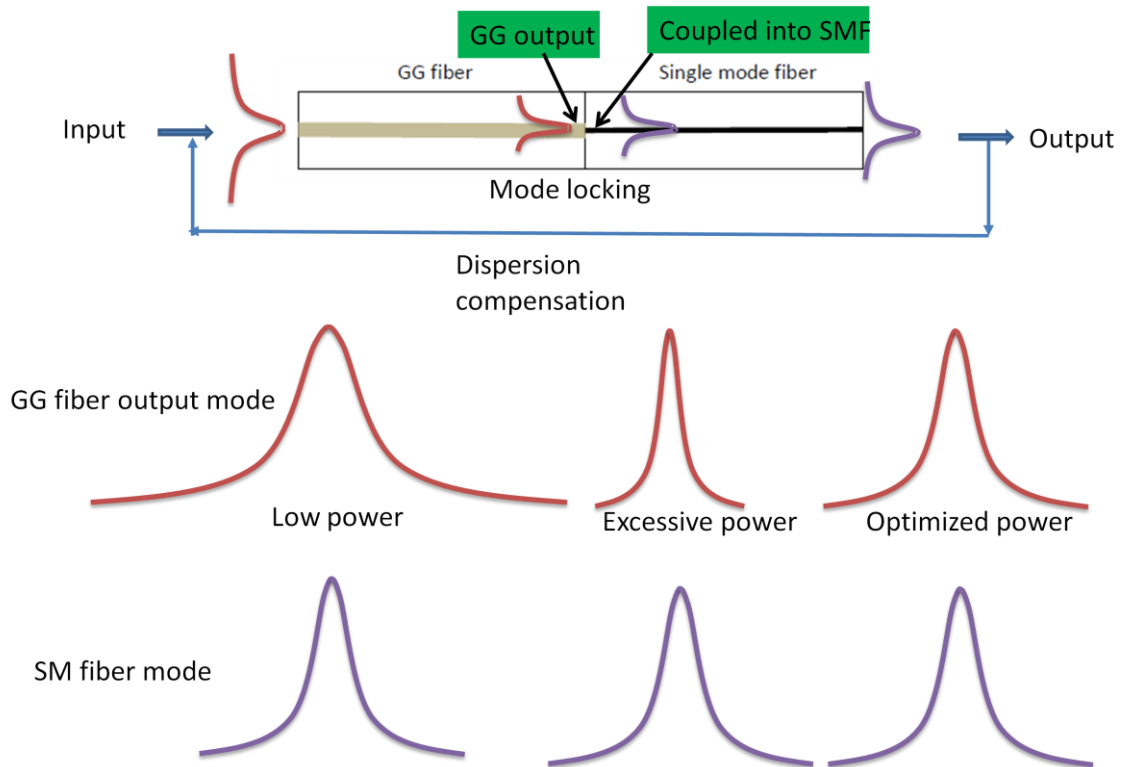


Figure 2-5. Illustration of Kerr-lens mode-locking with GG fiber and SMF fiber device.

Figure 2-5 illustrates Kerr-lens mode-locking with the GG and SMF fiber device. When the input power to the GG fiber is too low, then the GG fiber output mode width will be wider than the mode in the SMF. So the power coupling efficiency will be low. While if the input power to the GG fiber is too high, the GG fiber output mode width will be narrow than the mode in the SMF, which will still

result in low coupling efficiency. Only when the GG fiber output mode width matched with the SMF mode width, the coupling will be optimized. And this is where achieves KLM. Besides, mode size matching, dispersion caused by self-phase modulation also need to considered. Thus, additional dispersion compensation device such Fiber-Bragg grating and a standard single mode fiber may be needed to compensate the phase accumulated in the GG fiber.

2.5 Summary

Self-focusing, collapsing, and self-phase modulation effect in the GG fiber is studied by propagating a spatial-temporal pulse in the fiber and look at the pulse evolution at different distances. It is found that the temporal dispersion is caused by the spatial focusing and collapsing of the pulse. Following the GG fiber section, the pulse is coupled into a single mode fiber, the transmission characteristics of the power and phase are investigated. As the power launched into the GG fiber increases, the power coupling efficiency in the single mode fiber at low intensities is steady, then at intermediate intensities the coupling efficiency increases, and finally it becomes unstable as the field profile collapses at high intensities. The phase in the single-mode fiber is developed as the input power increases. A saturable absorber action of the transmission can be exploited to create mode-locking in a fiber cavity, i.e. Kerr lens mode-locking in fiber lasers for generating short pulses. Since the dispersion in the simulation is $-20 \text{ fs}^2/\text{mm}$, and the pulse width is 1 ps, the temporal dispersion length can be computed to be 50 meters, see Ref [25]. This is much longer than the fiber length we used. By shortening the pulse width to tens of fs the material dispersion length will be comparable or smaller than the GG fiber length, for example, a 10 fs half-width pulse has a dispersion length of 5mm. This situation will be explored in the context of a mode-locked fiber laser with a GG fiber section in the cavity.

CHAPTER III

DEVELOPMENT OF PHASE-LOCKING FIBER LASERS

Fiber lasers have many advantages over other type of lasers such as compactness, reliability, high-quality beams etc. Recently, fiber lasers also found to be suitable for the development of high power lasers. However, in a single fiber the power is limited by nonlinear effects such as stimulated Raman scattering and stimulated Brillouin scattering [20, 21], and also the optical surface damage. In this chapter, we propose an all fiber-based phase-locking fiber laser which coherently combines four fiber lasers together. The self-imaging which is caused by the Talbot effect in the fiber array cavity is studied, and the cavity design is proposed.

3.1 Self-imaging in waveguides

Self-imaging was first observed while people were studying the laser damage and power handling in optical fibers [34, 35]. Full-modal propagation analysis is probably the most comprehensive method to study self-imaging in

multi-mode waveguide. Let an input field profile be [36]

$$\psi_{(y,0)} = \sum_v c_v \psi_v(y) , \quad (3.1)$$

where v is the mode number, and the field excitation co-efficient c_v can be estimated using overlap integrals based on the field-orthogonality relations.

$$c_v = \frac{\int \psi_{(y,0)} \psi_v(y) dy}{\sqrt{\int \psi_v^2(y) dy}} . \quad (3.2)$$

Assuming the input field do not excite unguided modes, the input mode can be decomposed to:

$$\psi_{(y,0)} = \sum_{v=0}^{v=m-1} c_v \psi_v(y) \quad (3.3)$$

Then the field at a distance z can be written as the superposition of all the guided mode components, i.e.,

$$\psi_{(y,z)} = \sum_{v=0}^{v=m-1} c_v \psi_v(y) \exp[i(\omega t - \beta_v z)] \quad (3.4)$$

where β_v is the propagation constant of mode v . Taking the phase of the fundamental mode as a common factor for all the modes, pull it out from the summation. Also, drop the time dependent phase . Then Eq. (3.4) can be write as:

$$\psi_{(y,z)} = \sum_{v=0}^{v=m-1} c_v \psi_v(y) \exp[i(\beta_0 - \beta_v)z] \quad (3.5)$$

where

$$\beta_0 - \beta_v \cong \frac{v(v+2)\pi}{3L_\pi}, \quad (3.6)$$

and

$$L_\pi = \frac{\pi}{\beta_0 - \beta_1}, \quad (3.7)$$

is the the beating length of the lowest two mode. With Eq. (3.6) (3.7), at $z=L$, the field can be write as:

$$\psi_{(y,z)} = \sum_{v=0}^{v=m-1} c_v \psi_v(y) \exp\left[j \left(\frac{v(v+2)\pi}{3L_\pi}\right) L\right] \quad . \quad (3.8)$$

Now, let

$$\exp\left[j \left(\frac{v(v+2)\pi}{3L_\pi}\right) L\right] = 1 \text{ or } (-1)^v \quad . \quad (3.9)$$

The first conditions means at L , the field will repeat itself the same as its initial field, which is the so call self-imaging length. If the second condition is satisfied, the field at those L will be the direct replica for even modes and the mirror image of the intial field with respect to $y=0$ plane when the modes are odd. It can be shown that the first and second condition can be fullfilled at

$$L = p(3L_\pi), \quad p=0,1,2,3,\dots \quad (3.10)$$

for p even and p odd respectively.

The formation of multi-image is also possible. And the distance for multi-images are found to be at:

$$L = \frac{p}{2}(3L_\pi), p=1,3,5,\dots \quad (3.11)$$

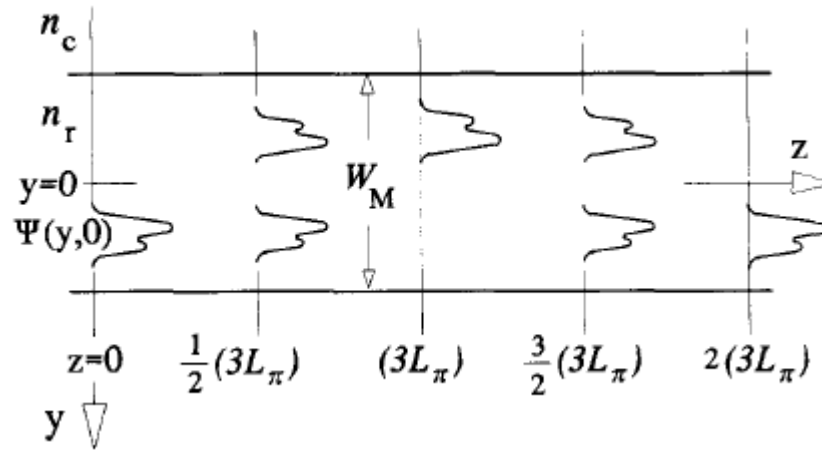


Figure 3-1. Multimode waveguide with mirror image at $3L_\pi$, direct image at $2(3L_\pi)$, and two fold images at $\frac{1}{2}(3L_\pi)$ and $\frac{3}{2}(3L_\pi)$. [36]

Until now the self-imaging has been demonstrated with full-modal propagation method, graphic illustration of the self-imaging is shown in Figure 3-1 [36]. The next section, we will numerically simulate the self-imaging in multimode waveguide.

3.2 Numerical simulation of self-imaging in fiber

In this section, I investigate self-imaging in optical fibers. Two Gaussian beams are couple into a multi-mode fiber; see Figure 3-2 for illustration. The fields for the beams are defined as:

$$A(x, z = 0) = A_{01,2} e^{-1(x-x_{1,2})^2/2w_{01,2}^2} , \quad (3.12)$$

where $x_{1,2}$ denote the locations of the beam centers, and $w_{01,2}$ denote the beam width. $A_{01,2}$ are the initial field amplitudes which have units of $2 W^{1/2} \cdot \mu m^{-1}$

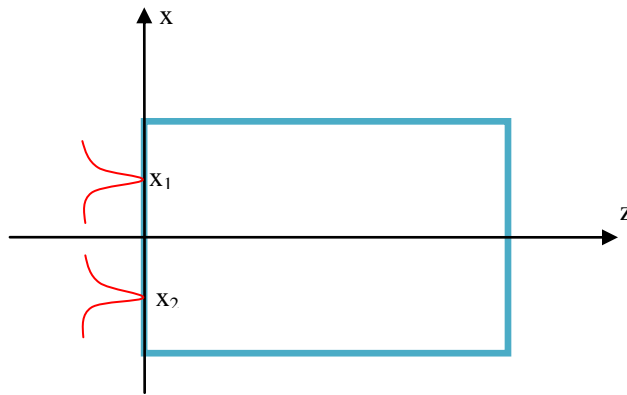


Figure 3-2. Illustration of two beams coupled into a multi-mode fiber. The beam centers are located at x_1 and x_2 respectively.

The beam propagation uses standard FFT, see Chapter 2 for details. The fiber parameters and the beam parameters are listed in Table 3-1. We propagate the beam for 14 mm in the fiber. The numerical simulation of beam evolution in the fiber is plotted in Figure 3-3. It is seen that both beams single self-image at about $z=14$ mm, and two self-image at about $z=7$ mm. The results confirmed the theoretical prediction of self-image in multi-mode fiber.

Parameter	Symbol	Value
Core index	n_{co}	1.5734
Cladding index	n_{cl}	1.5689
Core radius	r_{co}	100 μm
Cladding radius	r_{cl}	250 μm
Beam "1" center	x_1	30 μm
Beam "2" center	x_2	-30 μm
Beam "1" width	w_{01}	10 μm
Beam "2" width	w_{02}	10 μm
Initial field amplitudes "1"	A_{01}	$2 w^{1/2} / \mu\text{m}$
Initial field amplitudes "2"	A_{02}	$2 w^{1/2} / \mu\text{m}$

Table 3-1. The parameter of the multi-mode fiber and the beams coupled into the fiber for self-imaging.

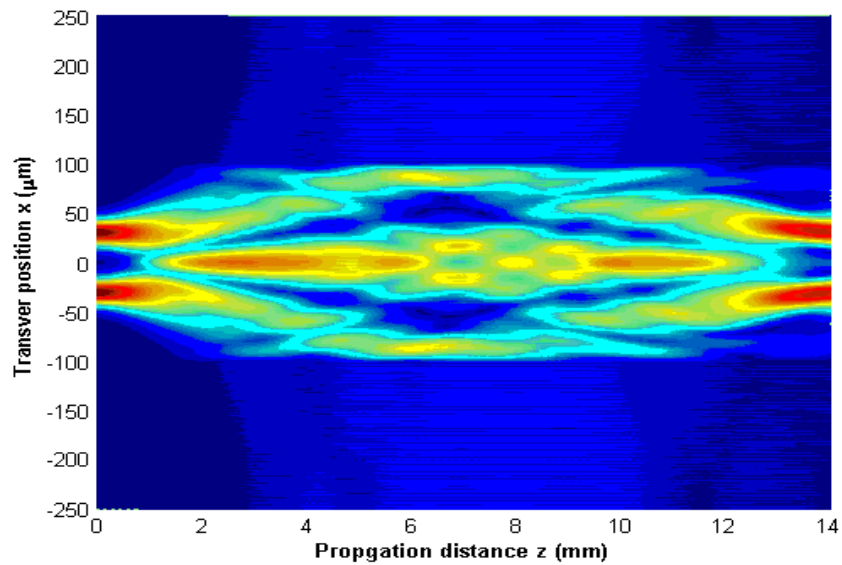


Figure 3-3. Self-imaging in MMF. The initial two Gaussian beams formed single self-imaging at about $z=14$ mm, and 2 double self-imaging at about $z=7$ mm.

3.3 Phase-locking fiber laser design

In this section a passive phased array fiber laser design based on self-imaging is proposed. This laser system design can be applied to develop Er-Yb doped phase-locking fibers lasers which can be pumped by the 50W diode laser with 975nm central emission wavelength available in our labs. The laser system can operate either in CW, active Q-switched, or passive mode-locked modes of operation. For this fiber laser system we need to fabricate a microstructured mirror on the end to control the cavity mode. The following chapter will show the modeling and simulation study for this phase-locking fiber laser system.

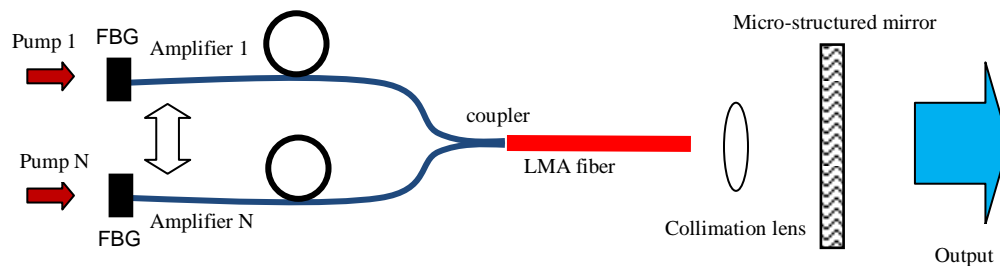


Figure 3-4. Phase-locked fiber laser system designs.

In Figure 3-4, a phase-locking fiber laser system is illustrated that is capable of phase-locking N fiber amplifiers. N fiber amplifiers are spliced together and coupled into a Large-mode-area fiber which served as the self-imaging device. Fiber Bragg-Gratings (FBGs) which pass the pump and reflect the signal serve as one end of the cavity mirror while the micro-structured mirror which reflect the self-images servers as the other end cavity mirror which also couples

the signal out. The collimation lens is used to collimate the signal comes from the LMA fiber.

For the simulation, I use 4 fiber amplifiers, and model the beam evolution in the LMA fiber, which is assumed to have a 200 micron core diameter. The simulation results are shown in Figures 3-5. We assume the starting beams in the LMA fiber are 4 Gaussian beams with the same parameters as the beams defined in section 3.2, see Figure 3-5(a). After propagating about 4.88 cm, the input beam profile is self-imaged; see Figure 3-5(c). I also plot the beam at $z=2.44$ cm (see Figure 3-5(b) for the beam distribution), and this is where we want to end the LMA fiber and put the micro-structured mirror. So in this way a self-consistent cavity for the phase-locking fiber laser system is formed.

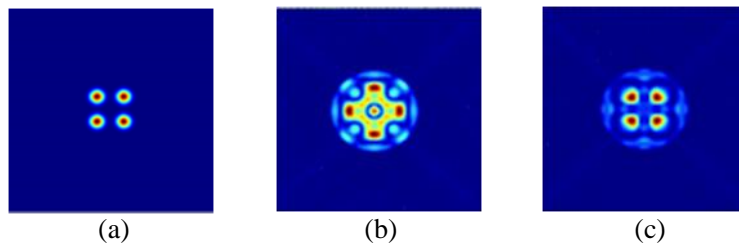


Figure 3-5. Simulation of self-imaging in LMA fiber of the phase-locking fiber laser system.

3.4 Summary

An all fiber-based phase-locking fiber laser is proposed in this chapter. This fiber laser is capable of generate high power output by coherent combination of signal from several fiber amplifiers. Self-imaging is simulated in the LMA fiber, the simulation result can be used to fabricate the micro-structured mirror. Furthermore, the amplifier might be made tunable along z direction to control the phase of each amplifier to change the position of self-imaging. Another possibility is to use wave-plates to rotate the polarization, which changes the coupling among the amplifiers to achieve lasing with single longitudinal modes [37].

CHAPTER IV

ERBIUM FIBER LASER GENERATING VECTORIAL BEAMS

In this chapter, I report the generation of CV beams using a *c*-cut calcite (calcium carbonate) crystal within a three-lens telescope in an erbium-doped fiber laser cavity. The use of a *c*-cut crystal generating azimuthal polarization was first demonstrated by Pohl in a Ruby laser cavity [38]. The author used hard stop in the cavity to stabilize the cavity which could reduce the efficiency of the laser system. However, it is not clear whether this method could be applied to a fiber laser cavity, since nonlinear and high birefringence in the fiber can aberrate the beam polarization state.

This chapter also investigates the polarization modes' behavior of this fiber laser cavity in details. The evolution of the mode polarization inside of the cavity is observed and reported. It is found that the mode polarization inside of the cavity can be spatially homogeneous in one section of the cavity while spatially inhomogeneous in another section of the cavity. This could open opportunities for other specifically nonlinear optical related processes that require polarization and phase matching. In addition, by translating the lens to

collimate rays between the ordinary and extraordinary foci, a generalized CV beam output that consists of a linear superposition of the radial and azimuthal polarizations has been obtained. Vectorial modes with more complicated spatial polarization distributions are also observed by creating angular misalignment of the axially symmetric birefringent element.

4.1 Introduction and development of Cylindrical Vector Beams

Unlike the commonly known spatially homogeneous polarizations such as linear, circular and elliptical polarizations, the state of polarization of laser beams with spatially variant polarizations depends on the spatial location of the beam cross section. Two special examples of spatially variant polarization that have attracted significant interest recently are radial polarization (RP) and azimuthal polarization (AP) with axially symmetric polarization distributions. The beams with such polarizations states have rotational symmetry in both field amplitude and polarization state. Due to its cylindrical symmetry, these beams are also called cylindrical vector (CV) beams. CV beams are solutions to Maxwell's equations that can exist in laser resonators, cylindrical waveguides, and free space [39].

When radially polarized beams are tightly focused by a high numerical aperture objective lens, spatially separated transverse and longitudinal field components are created and the longitudinal component is a nonpropagating

wave. The transverse spot size of the longitudinal component is found to smaller than the conventional diffraction limit. This unique focusing property has attracted interest and has led to many proposed applications. One category of application is high resolution imaging, by various means, such as, creating an ultra-small focal spot [40], using second-harmonic generation [41] third-harmonic generation [42] microcopies, dark field imaging [43], and coherent anti-Stokes Raman scattering (RP-CARS) microscopy [44]. Another important application of CV beams is optical trapping [45, 46]. At the same time, CV beams are also found suitable for material processing [47], and free space communications [48]. Recently, nonlinear optics with radially polarized beams has also been explored [49-52].

Various methods have been demonstrated to generate radially and azimuthally polarized beams. They can be categorized into active and passive methods. Active methods use polarization discrimination elements in the laser cavities to achieve the selection of radially or azimuthally polarized modes. The uses of birefringence crystals [38, 53-55] and conical Brewster angle prism [56] have been reported. For passive generation of circularly polarized vortex beams, the use of dichroic material [57], and a spiral phase plate to compensate the geometry phase have also been demonstrated [58-60].

Optical fibers have been widely used in many applications ranging from optical communications, electro-optics devices to sensor technologies. Recently,

generating CV beams with optical fiber has attracted increasing interests. Extra-cavity generation is relatively easy. Intra-cavity generation of CV beams is relatively difficult due to the strong nonlinearity of the fiber and strong field intensity in the cavity. The uses of a dual conical prism [61], an axicon [62, 63], and a spatially variable retarder [64] in a fiber laser cavity have been demonstrated. However, those polarization selection elements do not support high power, and they are not commercially available. In most of the cases, only one type of polarization is generated. Also, the beams quality is relatively poor.

4.2 Theoretical analysis

The generation of radial and azimuthal polarization in optical fiber laser cavity requires carefully choosing of fiber and the birefringent crystal. In the following sections, the fiber mode theory is revisited and the requirements on the optical fiber are analyzed. The birefringent crystal needs to provide sufficient spatial separation for the radial and azimuthal polarizations so that good discrimination can be achieved. Birefringent ray tracing results will be given to determine the optimal incident angle into the crystal in order to obtain the optimal separation.

4.2.1 Fiber modes

The modes that could be supported by fiber can be analyzed through the V-number which is defined as:

$$V = \frac{2\pi a}{\lambda} NA \quad , \quad (4.1)$$

where a is the core radius of the fiber, λ is the signal wavelength, NA is the numerical aperture of the fiber. Under weakly guided conditions, the modes can be described as linear polarized pseudo modes, i.e. LP modes. For a single mode fiber supporting only the fundamental mode, i.e., LP₀₁ mode has a V-number smaller than 2.405. The fundamental mode has an axially symmetric circular intensity distribution, and the field can be approximated as a Gaussian distribution if $V < 2.405$. This mode actually consists of two orthogonal linearly

polarized modes, i.e. HE₁₁ modes. If the V-number is bigger than 2.405 and smaller than 3.83, the fiber can also support the LP₁₁ mode groups. The degenerate modes of LP₁₁ are TE₀₁, TM₀₁, and HE₂₁. The intensity distributions for those modes have annular ring structures. The difference of the effective index of the modes in the fiber is very small under weakly guiding, so it is very hard to distinguish the modes through the intensity distributions. However, they have different polarization states. TE₀₁ denotes the azimuthally polarized mode; TM₀₁ denotes the radially polarized mode; and HE₂₁ denotes the hybrid mode without a symmetric polarization distribution. Under weakly guided condition, by solving the Maxwell's equation, the LP modes in the fiber can be approximated as [65]:

$$E(r, \phi) = \begin{cases} \frac{A J_l\left(\frac{Ur}{a}\right)}{U J_l(U)} \begin{pmatrix} \cos(l\phi) \\ \sin(l\phi) \end{pmatrix}, r \leq a \\ \frac{A K_l\left(\frac{Wr}{a}\right)}{W K_l(W)} \begin{pmatrix} \cos(l\phi) \\ \sin(l\phi) \end{pmatrix}, r > a \end{cases}, \quad (4.2)$$

where $J_l(x)$ is the l th order of Bessel function of the first kind, and $K_l(x)$ is the l th order of Bessel function of the second kind. $U = V\sqrt{1-b}$, and $W = V\sqrt{b}$, where b is the normalized propagation constant, and is given by the eigenvalue equation:

$$\frac{J_l(V\sqrt{1-b})}{U J_{l-1}(V\sqrt{1-b})} + \sqrt{\frac{1-b}{b}} \frac{K_l(W)}{W K_{l-1}(W)} = 0. \quad (4.3)$$

From Eq. (4.3), if V is given, the normalized propagation constant b for LP₀₁ and LP₁₁ can be found. So the field and intensity distributions can be

computed through Eq. (4.2).

The fiber used in our experiment is *LIEKKI*'s Er120-20/125DC fiber with emission spectrum centered near 1.6 μm . The numerical aperture $NA=0.09$, and the core radius is 10 μm . Thus the V -number can be found through Eq. (4.1) which is about 3.534. Thus, it can support the LP_{01} and LP_{11} modes. From Eq. (4.3), the b values are calculated to be 0.725, and 0.333 respectively. The intensity distributions of the modes in the fiber is plotted by using Eq. (4.2), see Figure 4-1 for the intensity distributions for LP_{01} , and LP_{11} mode.

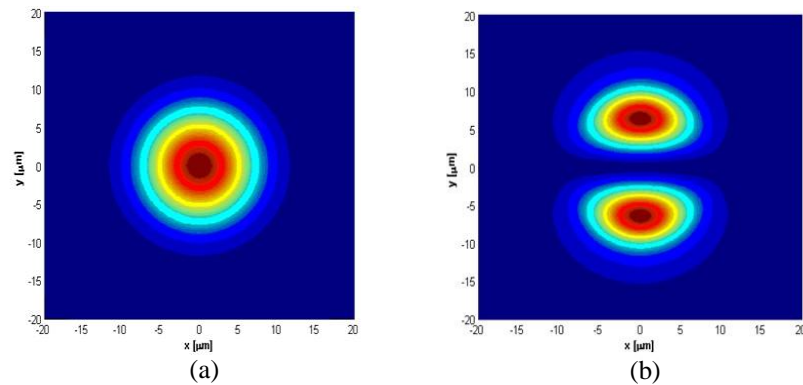


Figure 4-1. Intensity distributions of the fiber modes of erbium-doped fiber used in the experiment. (a): LP_{01} mode intensity distribution; (b): LP_{11} mode intensity distribution. The unit for x, and y axis is μm .

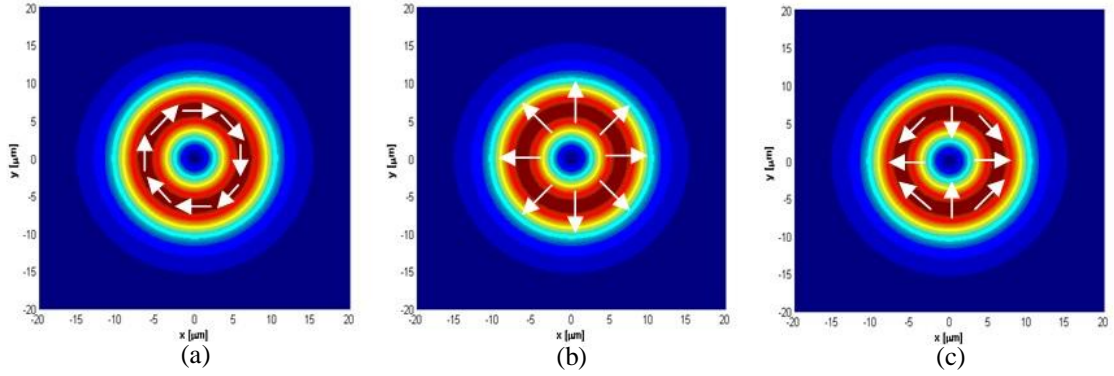


Figure 4-2. Intensity and polarization distributions for the degenerated LP₁₁ modes. (a): representation of TE₀₁ mode with azimuthal polarization; (b): representation for the TM₀₁ mode with radial polarization; (c): representation for the hybrid mode with mixed polarization. The polarization distributions are indicated by white arrows. The unit for x, and y axis is μm.

The LP₀₁ modes are linearly polarized modes with a central peak in the transverse plane. The LP₁₁ mode consists of three degenerate modes: TE₀₁, TM₀₁, and HE₂₁. All the degenerate modes are obtained by dropping the angular dependence when $l=1$. The intensity and the polarizations distributions are shown in Figure 4-2. Note that the HE₂₁ mode consists of two degenerate modes, and the other one has a polarization distribution rotated by 45 degrees compared with the one shown in Figure 4-2(c).

The intensity distributions for LP₀₁ and LP₁₁ modes can also be approximated by the Laguerre-Gaussian function, which is used to describe the modes in free space. At the beam waist the field distribution can be written as [66]

$$E(r, z = 0) = E_0 \left(\sqrt{2} \frac{r}{w_0} \right)^l L_p^l \left(\sqrt{2} \frac{r^2}{w_0^2} \right) e^{-i \left(-\frac{k}{2q_0} - l\phi \right)} \quad , \quad (4.4)$$

where w_0 is the beam size at the beam waist, $L_p^l(x)$ is the Laguerre polynomials,

q_0 is the beam parameter at the beam waist which is $q_0 = \frac{j\pi w_0^2}{\lambda}$. When $l=p=0$, this is reduced to the LP₀₁ mode. For $l=0, p=1$, it is reduced to the degenerated LP₁₁ modes.

4.2.2 Birefringence crystal for polarization selection

From the analysis of the fiber modes, it can be seen that the selection of radial or azimuthal polarization from the LP₁₁ modes group is intrinsically difficult, since the three degenerate modes have very slight difference in spatial distributions. Fortunately, those modes have different spatially variant polarization states that can be explored for mode selection. In this work, this selection is done with a *c*-cut uniaxial crystal. A *c*-cut (or *z*-cut) uniaxial crystal has different index for extraordinary and ordinary polarizations. When those beams are focused through the crystal, they will be spatially separated, see Figure 4-3(a) for illustration.

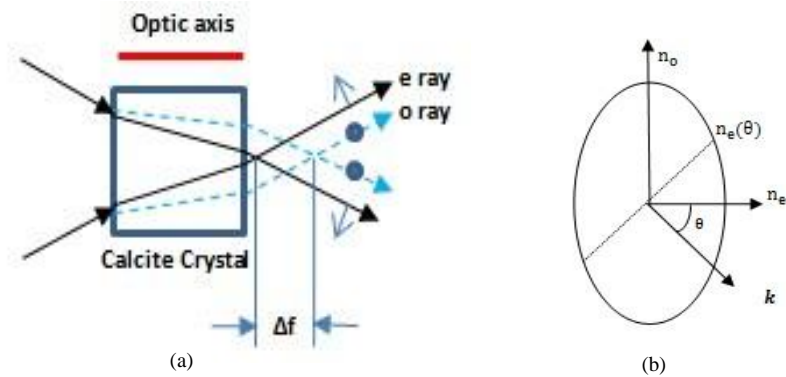


Figure 4-3. Illustration of birefringence crystal angular separation of radial and azimuthal polarizations. (a): The ray traces through the birefringence crystal; (b): The index ellipsoid of the calcite crystal. The calcite crystal is negative uniaxial crystal with $n_o=1.633$, and $n_e=1.478$ at $1.6\ \mu\text{m}$ wavelength.

In order to spatially separate different polarizations, the incident angle at the crystal interface is of great importance. At low incident angle, both polarizations will be focused far away from the calcite crystal and the separation of the two foci will be large. However, the depth of focus of both foci will be extremely large too, making the two foci connected and indistinguishable. In addition, we don't want the foci to be too far away from the crystal which may result in an extremely long cavity. As the incident angle increases, the two foci are closer to the crystal and the distinction becomes clearer due to the reduced depth of focus. However, the separation between the foci also drops. The separation between the two foci cannot be too small which will make the switching between the polarizations hard. Thus, there should exist an optimal incident angle for the optimal foci separation.

For ordinary ray, the refractive index is n_o , while for extraordinary ray, the

refractive index depends on the internal angle between the wavefront direction and the optical axis for a c-cut crystal. From the index ellipsoid equation, we have [67]:

$$\frac{1}{n_e^2(\theta_e)} = \frac{\cos^2(\theta_e)}{n_o^2} + \frac{\sin^2(\theta_e)}{n_e^2} \quad . \quad (4.5)$$

At the incident interface, from Snell's law of refraction, we have:

$$n_{air} \sin(\theta_{in}) = n_o \sin(\theta_o) = n_e(\theta_e) \sin(\theta_e) \quad (4.6)$$

From Eq. (4.5) and Eq. (4.6), the wavefront directions for ordinary and extraordinary rays can be obtained as:

$$\theta_o = \sin^{-1}(\sin(\theta_{in}) / n_o) \quad , \quad (4.7)$$

and

$$\theta_e = \sin^{-1}\left(\frac{\sin(\theta_{in}) \cdot n_e}{\sqrt{n_o^2 n_e^2 + n_e^2 - n_o^2}}\right) \quad . \quad (4.8)$$

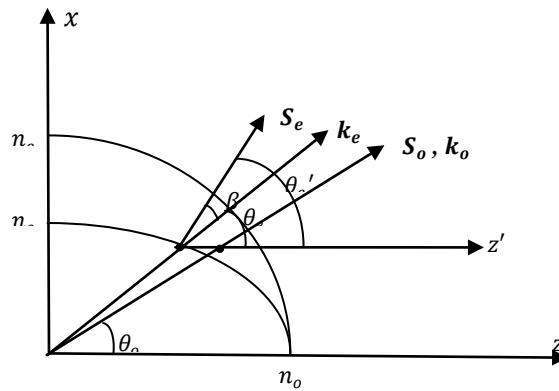


Figure 4-4. Normal surface of the calcite crystal used for describe the wavefront and energy flow directions.

However, the wavefront direction for the extraordinary ray is not the same

direction as the energy flow direction, i.e. the Poynting vector direction. In order to calculate the energy flow direction for the extraordinary ray, the normal surface is used as shown in Figure 4-4. In the figure, the energy flow for the extraordinary ray has a walk-off angle β with respect to its k vector which further separate this ray way from the ordinary ray. While for the ordinary ray, the wavefront and the energy flow travel in the same direction. The actual ray goes in the energy flow direction, thus the walk-off angle is important for knowing the actual separation of the extraordinary and ordinary beams. From the boundary conditions we have:

$$\tan(\theta'_e) = \frac{n_o^2}{n_e^2} \tan(\theta_e) \quad , \quad (4.9)$$

where θ'_e is the angle between the energy flow and the z-axis, and θ_e is the angle between the wavefront and the z-axis of the extraordinary ray. The walk-off angle is:

$$\tan(\beta) = \tan(\theta'_e - \theta_e) = \frac{\tan(\theta'_e) - \tan(\theta_e)}{1 + \tan(\theta'_e) \tan(\theta_e)} = \left(\frac{n_o^2}{n_e^2} - 1 \right) \frac{\tan(\theta_e)}{1 + \frac{n_o^2}{n_e^2} \tan^2(\theta_e)} \quad . \quad (4.10)$$

It can be shown that the walk-off angle is always much bigger than the separation angle of the wavefronts of the extraordinary and ordinary ray. The total separation angle of the energy flow directions for extraordinary and ordinary rays is:

$$\alpha = d\theta + \beta, \quad (4.11)$$

where $d\theta$ is the wavefront separation angle which is:

$$d\theta = \theta_e - \theta_o. \quad (4.12)$$

In Figure 4-5(a), the separation angle of the wavefront, energy flow, and the walk off angle are plotted as a function of the incident angle. The green curve is the total separation angle (energy flow separation), the blue curve is the walk-off angle, and the red curve is the wavefront separation angle. It can be seen that the walk-off angle is much higher than the wavefront separation angle.

The angle of the energy flow for the extraordinary is $\theta_e + \beta$ and energy flow direction for ordinary rays is the same as the wavefront direction. Refer to Figure 4-3(a), and through simple trigonometry, the separation of foci can be calculated as:

$$\Delta f = \frac{2 \times L \cdot (\tan(\theta_e + \beta) - \tan(\theta_0))}{\tan^2(\theta_{in})}, \quad (4.13)$$

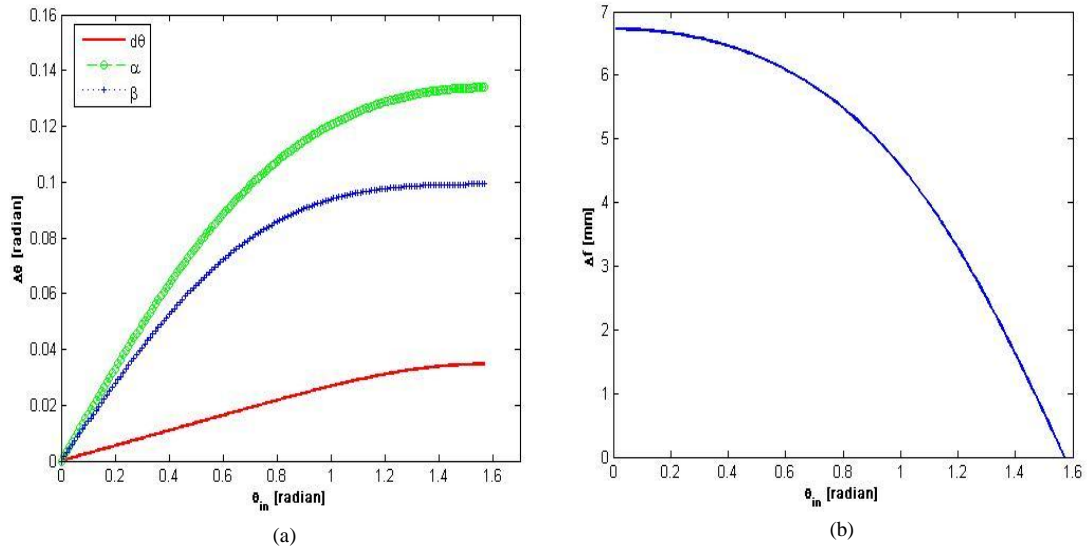


Figure 4-5. Plot of separation angle of the wavefronts and energy flows for ordinary and extraordinary rays, and the foci separation as a function of incident angle. (a): Plot of the separation and wavefronts and the energy flow, and the walk-off angle as a function of function. The unit of x and y axis is radian; (b): Plot of the foci separation as a function of incident angle. The x axis unit is radian, and the y axis unit is mm.

where L is the crystal length which is 20 mm (the length of the c -cut calcite cube we use in this work). The foci separation is plotted as a function of the incident angle in Figure 4-5(b). From the plot, it is found that, the separation falls as incident angle increases. However, if the incident angle is too small, the rays after the crystal will be converged to points very far away from the crystal which makes the cavity too long, thus less compact and hard to align. If the incident angle is too large, then the separation will be too small which would require a fine translation stage for the collimation lens to achieve polarization switching.

4.3 Experimental generation of Vectorial Beams

In this chapter, we first demonstrate generation of radially and azimuthally polarized beams from the fiber laser cavity. And the polarization output can be made interchangeable between radial and azimuthal polarization. The maximum output power exceeds the reported record of fiber laser CV beams generations. Additionally, we studied the polarization evolution throughout the cavity. And it is found that the polarization at one end of the cavity is CV beams output while the other end is linearly polarized output. Moreover, when both radial polarization and azimuthal polarization in the cavity achieve lasing simultaneously, interesting polarization patterns are obtained.

4.3.1 Experimental generation of Cylindrical Vectorial Beams

The experimental setup is illustrated in Figure 4-6. A 4-meter long Erbium doped double cladding fiber with $NA=0.09\pm 0.01$ and 20 μm core diameter (LIEKKI Er120-20/125DC, emission spectrum centered near 1.6 μm) is used as the gain medium in the laser cavity. The fiber is carefully chosen so that it can support the fundamental mode, and the second higher order modes, i.e., the radially polarized mode (TM_{01}), azimuthally polarized mode (TE_{01}), and the hybrid mode (HE_{21}). A 976 nm diode pump laser (Visotek DL series) is end-coupled into the Erbium doped fiber using lens L1 ($f_1=25$ mm) and lens L2 ($f_2=8$ mm) with the dichroic mirror inserted in between. The dichroic mirror is highly transmissive for the pump and highly reflective for the signal. Mirror M1 (100% reflectance at 1.6 μm) and the output coupler M2 (80% reflectance at 1.6 μm) are the end mirrors for the laser cavity. Lens L3 ($f_3=6$ mm) is used to collimate the output from the fiber. Negative lens L4 ($f_4=-25$ mm), lens L5 ($f_5=38.1$ mm), and lens L6 ($f_6=19$ mm) form a telescope system with the c-cut calcite crystal inserted between L5 and L6. The crystal axis of the c-cut calcite is aligned with the optical axis of the cavity to select either radial or azimuthal polarization modes in the cavity. Due to the negative birefringence of calcite and the rotational symmetry, ordinary (azimuthal polarization) and extraordinary (radial polarization) modes will be focused to different foci after the calcite crystal. Lens L4 is used to expand the beam such that we can use lens L5 to focus the beam

into the calcite crystal with a larger incident angle. This is necessary to generate a sufficiently large refractive index difference for the extraordinary (radial polarization) and ordinary (azimuthal polarization) beams with respect to the calcite crystal, consequently producing a larger separation of the foci for radial and azimuthal polarization. By translating L6 along the optic axis (indicated in Figure 4.6), we can select either the radially or azimuthally polarized modes to be collimated. The collimated polarization will experience lower loss in the cavity and can thus start to oscillate. Illustrated in Figure 4-6, the azimuthally polarized beam is collimated and consequently selected as the output mode. If we simply move L6 slightly to the right along the optical axis, then the radially polarized mode will be collimated instead and the output will be switched from the azimuthal polarization to the radial polarization.

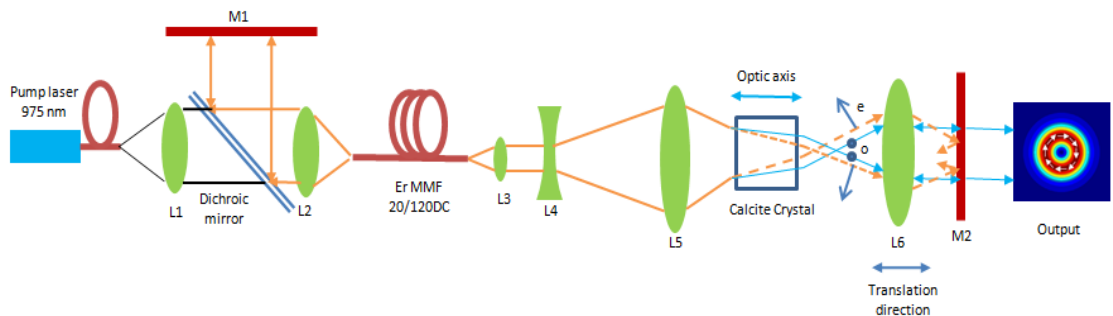


Figure 4-6. Experiment setup of an Erbium doped fiber laser generating radially or azimuthally polarization. The solid rays indicate ordinary beams (azimuthal polarization), and the dashed rays indicates extraordinary rays (radial polarization).

Beam profiles are recorded at the pump power of 2.8 W. The images of the beam profiles are recorded with an InGaAs NIR Camera (Indigo Merlin™).

The azimuthally polarized output is represented in Figures 4-7. Figure 4-7(a) is the output mode intensity distribution. A linear polarizer is put before the camera to check the polarization; the modes after the polarizer are shown in Figures 4-7 (b)-(e). The transmission axis of the linear polarizer is indicated by the white arrows. It can be concluded from Figures 4-7, an azimuthally polarized mode is generated from the fiber laser cavity. A line scan across the center of the generated mode is also plotted with comparison to the theoretical radially polarized LG_{01} mode profile. The diameter of the beam is measured to be 1.0 mm. Then we moved L6 in the setup about 0.6 mm to the left to collimate the extraordinary beam, i.e. radially polarized beam, the measurements of the beam is shown in Figures 4-8(a)-(e) which indicate a radially polarized beam has been obtained. The beam diameter measured is 0.8 mm instead. The switching between radial and azimuthal polarizations has been successfully demonstrated.

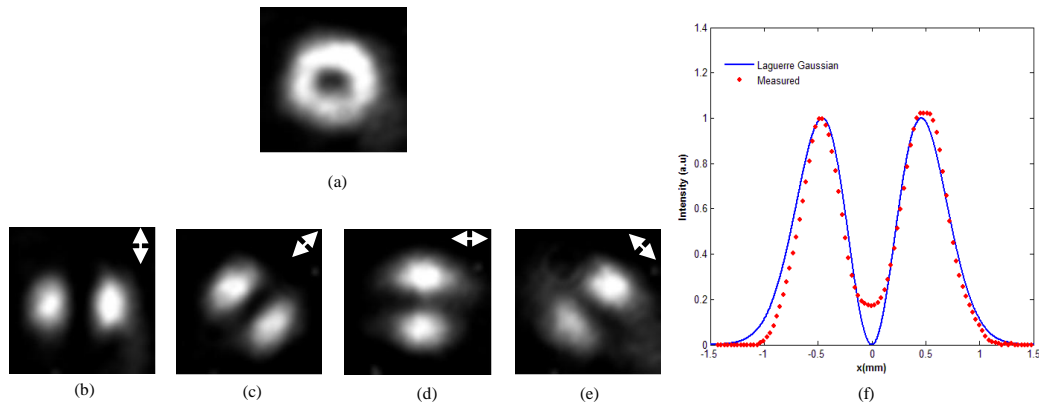


Figure 4-7. Measurements of the azimuthally polarized mode, and linescan comparisons between the experiment and theory. (a): Intensity distribution of the output beam; (b)-(e): intensity distributions after a linear polarizer. The polarizer transmission axis is indicated by white arrows; (f) linescans comparison between the experimental result and the theoretical prediction. The theoretical curve is calculated with a Laguerre Gaussian distribution. The unit of x axis is mm, and the y axis intensity peak is normalized to unity.

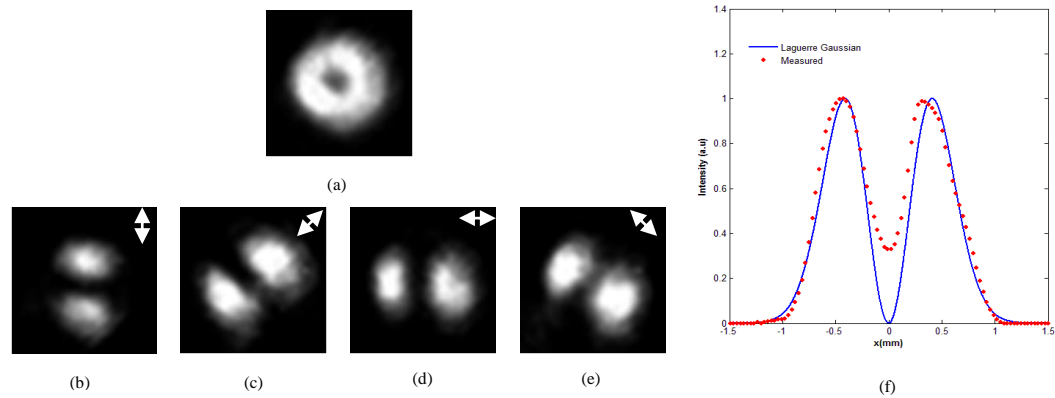


Figure 4-8. Measurements of the radially polarized mode, and linescan comparisons between the experiment and theory. (a): Intensity distribution of the output beam; (b)-(e): intensity distributions after a linear polarizer. The polarizer transmission axis is indicated by white arrows; (f) linescans comparison between the experimental result and the theoretical prediction. The theoretical curve is calculated with Laguerre-Gaussian distribution. The units of x axis is mm, and the y axis intensity peak is normalized to unity.

The signal output power as a function of the launched pump power for both azimuthally and radially polarized modes is also measured (Figure 4-9).

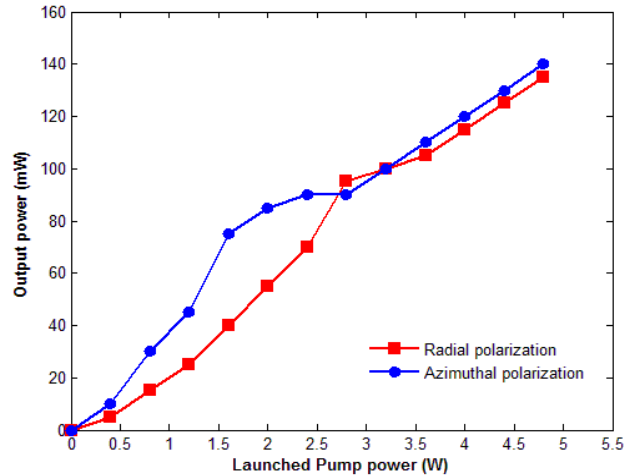


Figure 4-9. Output power vs. the launched pump power.

During the measurement, the mode profiles for radial and azimuthal polarization are maintained at good quality. The maximum output power for radial polarization is about 135 mW and 140 mW for azimuthally polarization. To our best knowledge, this is the highest output power level for a fiber laser that produces CV beams. The threshold of the fiber laser is found to be about 0.2 W and the slope efficiency of our fiber laser is 2.85% and 3.09% for radial and azimuthal polarization respectively. The slope efficiency may be further improved by optimizing the fiber laser cavity design in the future. For example, optimal fiber length needs to be determined in order to improve the slope efficiency. If the fiber is too long, the signal will be absorbed by the fiber when it travels in the backward direction in the fiber. While if the fiber is too short, the pump power will

be wasted. Also, the pump coupling system needs to be improved to make the numerical aperture and the beam size to be matched between the pump laser and the erbium-doped fiber. Other design parameters that could be further optimized to include the reflectance of the output coupler, the wavelength of the diode pump laser, etc.

4.3.2 Polarization evolution in fiber laser cavity

The fiber system used in the experiment is illustrated in Figure 4-10. The details of the setup are described in Chapter 4.3.1. In Figure 4-10, radial polarization output mode intensity as measured by an infrared camera (Indigo Merlin™) is donut shaped, which is shown as inset. Azimuthal polarization output intensity was also observed by translating L6 to the right about 1 mm to collimate the rays near the ordinary focus. The polarization evolution in the cavity is

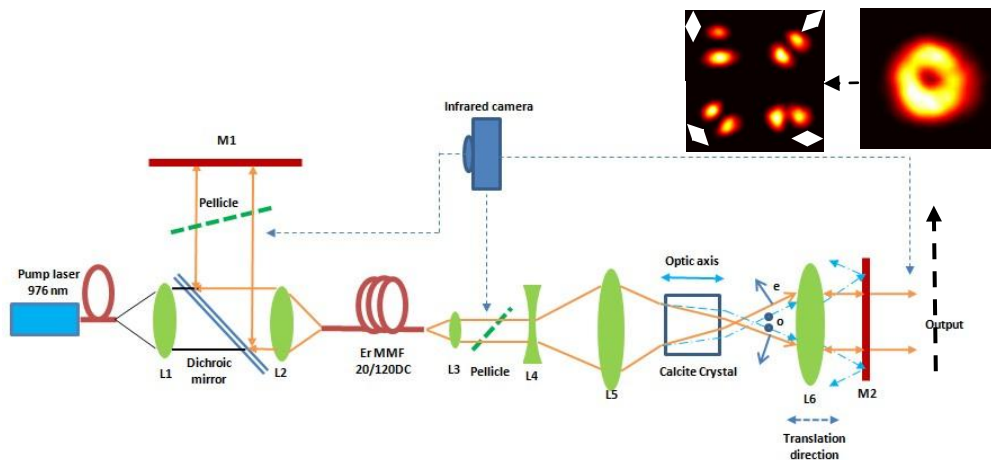


Figure 4-10. Illustration of the vectorial fiber laser design with a c-cut calcite crystal and a three-lens telescope in the cavity. An example of radial polarization mode intensity generated with this laser is shown at the top right inset photo. A series of four photos after inserting a linear polarizer is short on the top left inset.

studied when the laser produces radial or azimuthal polarization outputs. Besides measuring the output polarization, the polarization states in front and after the fiber are also measured. The measurements are done by putting a pellicle in the cavity at different locations (indicated in Figure 4-10). With an IR camera and a linear polarizer, the polarization states at those locations are analyzed.

I first examine the polarization in the cavity when the output is radially polarized. A pellicle is inserted between L3 and L4 with the surface of the pellicle is rotated by about 45° with respect to the optical axis. Ideally this angle needs to be very small to reduce the difference in reflectance for s- and p-polarizations. However, this was not possible for us due to the relatively large aperture size of the pellicle (2 inches) and a very tight space between L3 and L4. The incident angle we use is very close to the Brewster's angle (for polymer with index of refraction of 1.47, the Brewster's angle is 55.8°) where the p-polarization has reflectance nearly zero. This needs to be taken into considerations for the polarization analysis in this part.

The beam profile is recorded with the infrared camera and the polarization is analyzed by rotating a linear polarizer in front of the camera (shown in Figures 4-10). Figures 4-11(a)-(c) are the measurements for the beam exiting from the fiber end. Figure 4-11(a) is the beam profile without passing through the linear polarizer, and Figures 4-11(b) and (c) are the beams with a linear polarizer. The polarizer transmission axis is indicated by the white arrow. For radial polarization the right and left sides of the beam are p-polarized will be extinguished by the pellicle at an incident angle near Brewster's angle, leaving the top and bottom

parts that are s-polarized. Figures 4-11(b) and (c) further confirm that the polarization of the beam reflected by the pellicle is mostly vertical. Similarly, the polarization state of the beam back to the fiber is measured, and the results are shown in Figures 4-11(d)-(f). From these measurements we conclude that, between L3 and L4, the polarization states in both directions between the fiber and the output mirror are radial polarizations, which is expected from the self-consistent requirement of laser theory.

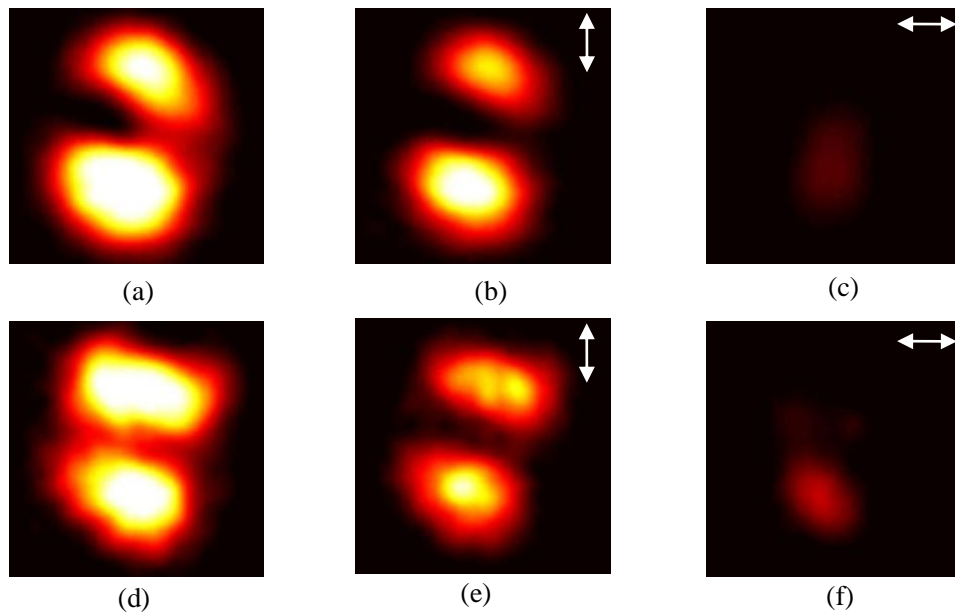


Figure 4-11. Polarization states between L3 and L4 when the output is radial polarization. (a)-(c) represent the beam from the fiber; (a) the initial the beam from the fiber, (b) and (c) are the beams after a linear polarizer; (d)-(f) represent the beam from the crystal back into the fiber; (d) the initial beam without linear polarizer, (e) and (f) are the beams after a linear polarizer. The linear polarizer axes are indicated by white arrows.

Similarly, the polarization states between L3 and L4 are examined for azimuthal polarization output (shown in Figures 4-12). Compared with Figures 4-

11, the beam profile without passing through linear polarizer becomes two horizontal spots. This is because for azimuthal polarization the top and bottom parts are p-polarized with respect to the pellicle. Thus, at incident angle close to the Brewster's angle, the left and right parts are reflected. The polarization direction measurements with a linear polarizer confirmed this conclusion.

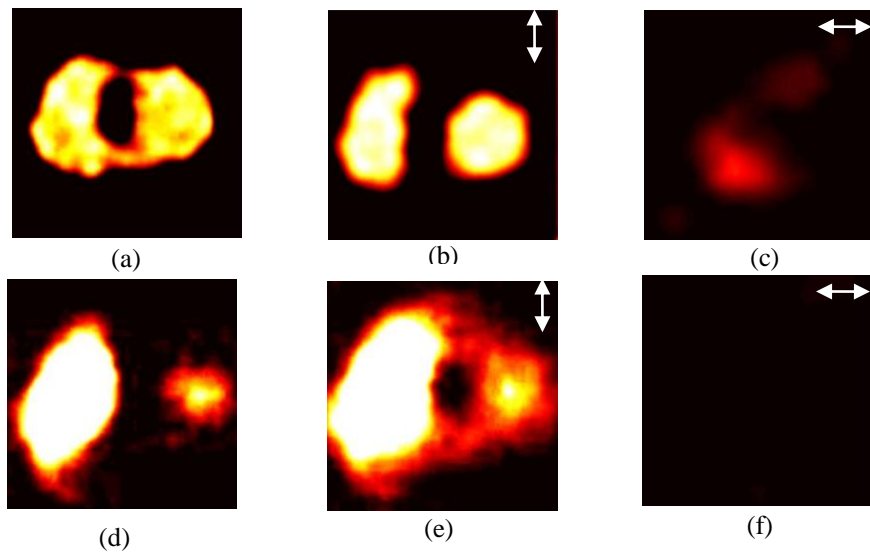


Figure 4-12. Polarization states between L3 and L4 when the output is azimuthal polarization. (a)-(c) represent the beam from the fiber; (a) the initial the beam from the fiber, (b) and (c) are the beams after linear polarizers; (d)-(f) represent the beam from the crystal; (d) the initial beam from the crystal, (e) and (f) are the beams after linear polarizers. The linear polarizer axes are indicated by white arrows.

For radial and azimuthal polarization output, the polarization states between M1 and the dichroic mirror (see Figure 4-10) are also measured by using the same pellicle. In this case the incident angle on the pellicle is adjusted to be very small to minimize the difference in reflectance for s-polarization and p-polarization since there is sufficient space between M1 and the dichroic mirror.

The experimental results show the beam profile for both cases are nearly a Gaussian and the polarization states are linear (see Figures 4-13). Figures 4-13(a)-(c) show the measurements corresponding to radial polarization output and Figures 4-13(d)-(f) are for azimuthal polarization output. Notice that the orientations of the linear polarization corresponding to the radial and azimuthal polarization outputs have approximately 45° angle with respect to each other. The linear polarization state near M1 is also verified by directly inserting a linear polarizer between M1 and the dichroic mirror. When the polarizer axis is rotated to be the same as the measured axis of linear polarization, the CV beams output profile and polarization at M2 is maintained to be either radial or azimuthal, which again confirms the linearly polarized beam at this end of the cavity.

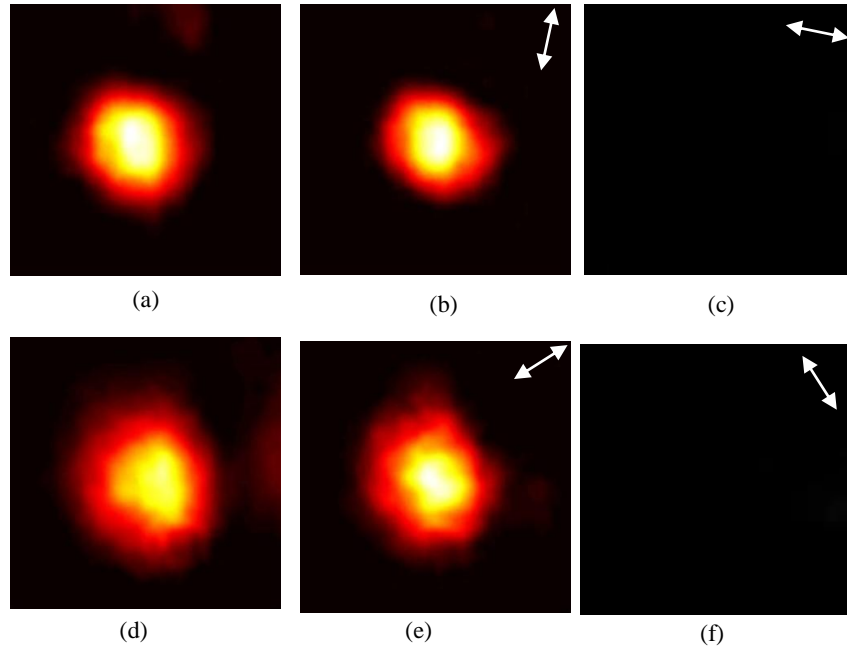


Figure 4-13. Polarization states in the cavity in front of M1 for radial and azimuthal polarization outputs. (a)-(c) and (d)-(f) represent the polarization states for radial and azimuthal polarization outputs respectively. The linear polarizer axes are indicated by white arrows.

4.3.3 Generation of generalized cylindrical vector output

In Figure 4-10, we used the rim rays to draw two distinctively separated foci corresponding to the radial and azimuthal polarization to illustrate the working principle of this fiber laser design. In reality, the two foci are connected as a continuous caustic zone with the near axis rays being included. If we translate lens L6 such that its front focal point is located in the middle of the two foci for the rim rays, then both radial and azimuthal polarization could oscillate simultaneously in the cavity, producing a generalized cylindrical vector beam with the local polarization pointing with certain angle between the radial and azimuthal directions. This is confirmed experimentally (see Figures 4-14). The

overall beam intensity profile is shown in Figure 4-14(a). The beam profiles after a linear polarizer are shown in Figures 4-14(b)-(d). From these measurements we can calculate the local polarization direction which is illustrated with those black arrows superimposed on Figure 4-14(a). In this case, it is found that the local polarization points at approximated 30° away from the radial direction and the polarization distribution maintains cylindrical symmetry. The radial and azimuthal components superimpose to each other and result in a generalized polarization state as we expected.

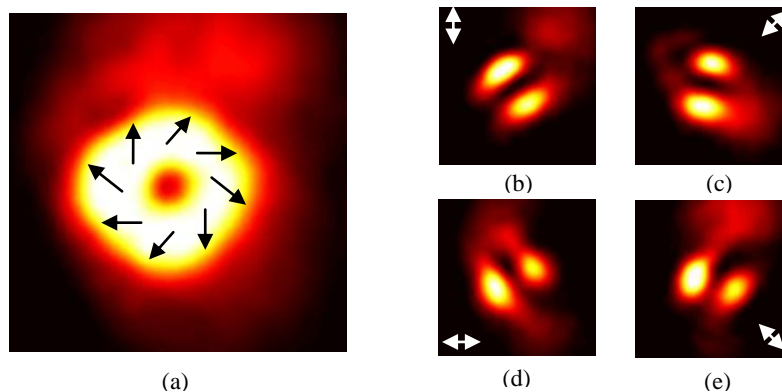


Figure 4-14. Generation of generalized cylindrical vector polarization. (a) the output beam intensity profile; (b)-(e) the intensity profiles after a linear polarizer whose transmission axis is indicated by the white arrows.

4.3.4 Vectorial vortex mode generation with angular misalignment

For the experiments described above, the c-cut calcite crystal is carefully aligned with the three-lens telescope and the cavity. However, if the calcite crystal is intentionally misaligned angularly while lens L6 focuses in the middle of the two foci, complicated polarization vortex structures are observed. One of

such example is shown in Figure 4-15. Figure 4-15(a) is the output beam profile which still exhibits a donut shape with larger dark core. However, the beam after a linear polarizer has a 4-lobe pattern and the pattern does not follow the rotation of the linear polarizer (Figures 4-15(b)-(e)). Apparently, the polarization of this output mode is no longer cylindrically symmetric.

The observed patterns can be phenomenological explained by the linear superposition of radially polarized and azimuthally polarized modes with opposite topological charges [66]. Assuming the radial and the azimuthal polarizations have the same Laguerre Gaussian profile with opposite topological charges +1 and -1 respectively; these two components can be written as:

$$E_r(r, z = 0) = A_{ra} \left(\sqrt{2} \frac{r}{w_0} \right) \exp\left(-\frac{r^2}{w_0^2}\right) e^{+i\varphi} e^{i\varphi_1} \hat{\mathbf{e}}_r, \quad (4.14)$$

$$E_\varphi(r, z = 0) = A_{az} \left(\sqrt{2} \frac{r}{w_0} \right) \exp\left(-\frac{r^2}{w_0^2}\right) e^{-i\varphi} e^{i\varphi_2} \hat{\mathbf{e}}_\varphi, \quad (4.15)$$

where w_0 is the beam size at the beam waist; φ is the azimuthal angle with respect to the positive x-axis direction; $e^{-i\varphi}$ and $e^{+i\varphi}$ are the spiral phase terms and $e^{i\varphi_1}$ and $e^{i\varphi_2}$ take account the phase differences due to the wavelength difference and path difference for each polarization in the cavity [68]. In our simulation we choose $\varphi_1 = \pi/4$ and $\varphi_2 = -\pi/4$. In order to perform coherent addition of both fields, the radial and azimuthal polarizations are decomposed into x- and y-axis as:

$$E_r = \cos\varphi \cdot E_r(r, z = 0) \hat{\mathbf{e}}_x + \sin\varphi \cdot E_r(r, z = 0) \hat{\mathbf{e}}_y, \quad (4.16)$$

$$E_\varphi = \sin\varphi \cdot E_\varphi(r, z = 0)\hat{e}_x - \cos\varphi \cdot E_\varphi(r, z = 0)\hat{e}_y. \quad (4.17)$$

The simulation results are shown in Figures 4-15. Figure 4-15(a) is the simulated output beam profile, while Figures 4-15(b)-(e) show the beam profiles after passing through a linear polarizer with transmission axis indicated by the white arrow. The simulation is able to repeat the general pattern of the experimental results shown in Figures 4-16.

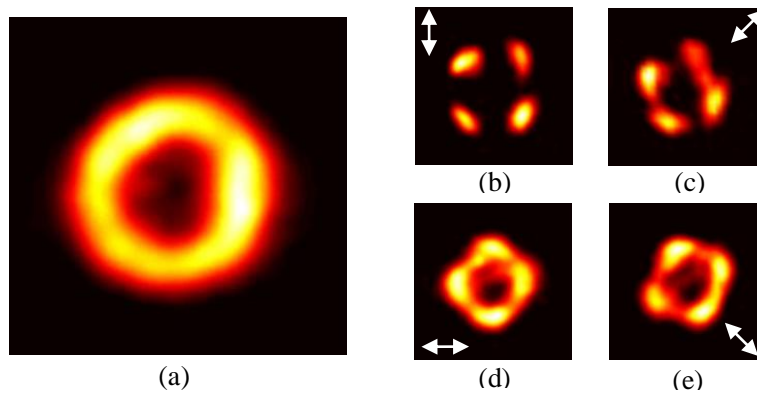


Figure 4-15. Experimental results of output mode with angular misalignment and four-spot patterns after polarizer. (a) the intensity profile of the output mode; (b)-(e) the beam intensity profiles after a linear polarizer whose transmission axis is indicated by the white arrow.

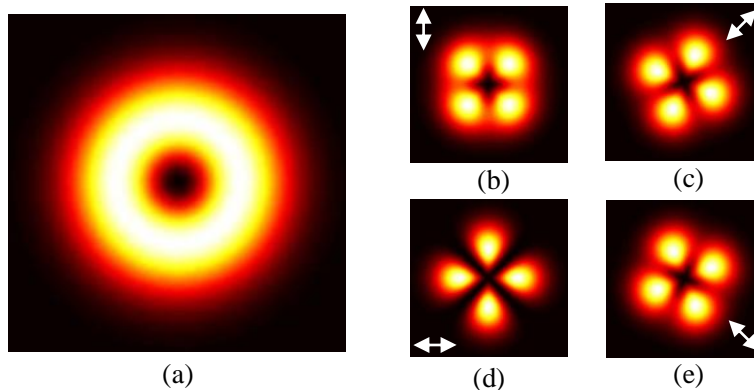


Figure 4-16. Numerical simulation results of the linear superposition of radial and azimuthal polarization with one opposite topological charge. (a) shows the overall intensity profile; (b)-(e) are the beam profiles after linear polarizer whose transmission axis is indicated by white arrows.

Experiment results of donut output modes with 6-lobe pattern after the linear polarizer have also been observed, see Figures 4-17. Numerical simulation of a linear superposition of radial and azimuthal polarizations with positive and negative spiral phase with topological charge of 2 are consistent with experimental observations, see Figure 4-18. However, the physical explanation of this observation is still under investigation.

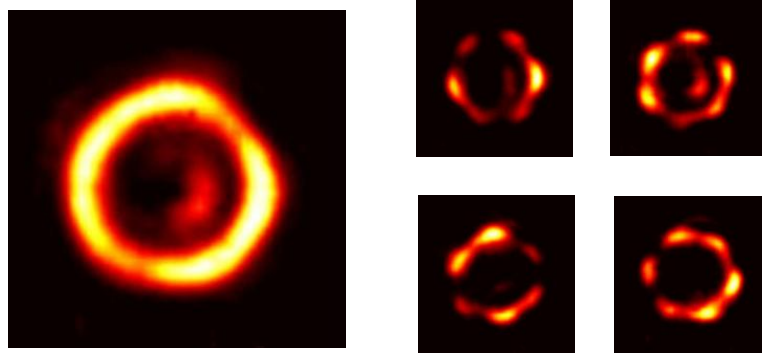


Figure 4-17. Experimental results of output mode with angular misalignment and six-spot patterns after polarizer. (a) the intensity profile of the output mode; (b)-(e) the beam intensity profiles after a linear polarizer whose transmission axis is indicated by the white arrow.

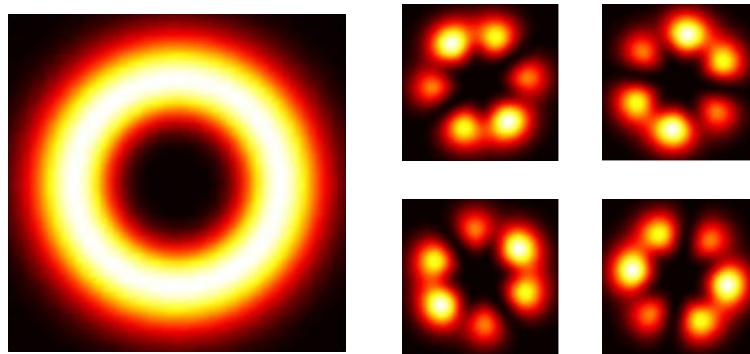


Figure 4-18. Numerical simulation results of the linear superposition of radial and azimuthal polarization with two opposite topological charges. (a) shows the overall intensity profile; (b)-(e) are the beam profiles after linear polarizer whose transmission axis is indicated by white arrows.

4.4 Summary

In this Chapter, a fiber laser with spatially variant polarization states has been experimentally constructed and the field distributions for radial and azimuthal polarizations in the cavity have been obtained. Our fiber laser cavity can be switched between the two polarization states by adjusting one lens. The ordinary ray (azimuthal polarization) and the extraordinary ray (radial polarization) behaviour in a *c*-cut calcite crystal have been studied with birefringence ray tracing and the foci separation of the rays after the crystal has been determined as a function of the incident angle. These forms the theoretical foundation of a fiber laser cavity design that can produce switchable radially and azimuthally polarized output modes. The maximum radial and azimuthal polarization power output is about 140 mW. The output power can be further improved by optimizing the pump laser wavelength, using an optimal fiber length, and choosing an optimal output coupler, as well as improving the pump coupling efficiency, etc.

I also reported the producing of reconfigurable vectorial output modes. The evolution of the mode polarization in the laser cavity has been investigated. The vectorial self-consistency condition within this cavity is confirmed by observing the polarization in both directions between the output mirror and the erbium doped fiber. It is also found that the erbium doped fiber performs a polarization mode conversion function in the cavity that allows the conversion

between a spatially homogeneous polarization state on one end of the fiber and a spatially inhomogeneous polarization states on the other end of the fiber [69].

In addition, by translating one of the intracavity lenses, both radial and azimuthal polarizations can oscillate simultaneously, producing generalized CV beam output directly. If angular misalignment is introduced to the birefringent crystal at this point, more complicated vectorial output modes have also been observed. We phenomenologically explained the observed complex polarization patterns of these donut shape vectorial modes as linear combinations of orthogonally polarized vectorial vortex beams with different topological charges. However, the exact underlying physical process that gives rise to such phenomena needs further investigation.

The findings reported here contribute to the understanding of the polarization dynamics and design issues of vectorial fiber lasers and demonstrate the rich polarization phenomena within a fiber laser cavity that could be exploited for applications. For example, the spatial separation of the spatially homogeneous and inhomogeneous polarization states in the same laser cavity is very interesting. Such a spatial separation may enable new fiber laser cavity designs. Vectorial laser modes with shorter wavelengths could be achieved by inserting nonlinear optical crystal in the part of cavity with linear polarization states to perform frequency conversion such as frequency doubling, a nonlinear optical process cannot be directly performed to the spatially inhomogeneous

states due to the requirements on polarization and phase matching.

Sources with such unusual beam polarizations can be suitable for applications in fiber communication, free space communication, and remote sensing technologies.

CHAPTER V

CONCLUSION AND FUTURE WORK

In the first chapter, I studied the Er-Yb fiber amplifiers. The pump dissipation and the signal amplification are simulated in the fiber by solving the rate equations. In the future, for the Er-Yb fiber laser system, the signal saturation effects also need to be considered. The simulation results can also be applied to wavelength tunable fiber laser development.

In the second chapter, GG fiber is introduced. The self-focusing, collapsing and self-phase modulation effects are investigated by propagating a spatial-temporal pulse in the fiber. Self-focusing of the pulse in the GG fiber makes this fiber possible for mode-locking. A GG fiber with a standard SMF is used to construct a fiber ring cavity which is proposed for making a Kerr-lens mode-locking fiber laser. It is found that by shortening the pulse, the temporal dispersion becomes significant in a very short GG fiber section. This temporal dispersion gives opportunities to balance the phase from the self-phase modulation in the GG fiber. Fiber Bragg-grating can also be added to this fiber laser cavity for flattening the phase of the pulse to avoid collapsing of the pulse. In the future, a more detailed mode-locked fiber laser system will be developed,

and the numerical algorithm for pulse propagation in the whole cavity will also be made complete.

In Chapter 3, a all fiber based phase-locked fiber laser is proposed. Self-imaging is simulated in the LMA fiber, and the result can be used to guided the fabrication of the micro-structured cavity mirrors in the future. In order to achive lasing and change the output characteristicstics, the pump lasers can also be maded tunable along z direction, and the polarization can also be controled by using waveplates.

In Chapter 4, CV beams generation is covered. A fiber laser system that is capable of generating both radial and azimuthal polarization output is demonstrated. The superposition of both radial and azimuthal polarization as an output is also achieved from this fiber laser cavity. Misalignment in the cavity which introduces opposite topological charges to both of the polarization components, and more generalized polarization patterns are obtained. Sources of these generalized CV beams will found applications in free space communications, remote sensing, etc. The polarization evolution throughout the fiber laser cavity is carefully investigated while the output is radial or azimuthal polarization. The founding that at the other end of the cavity, the polarization is linear will open access to nonlinear processes such as second harmonic generations. So in future studies, a nonlinear crystal like BBO crystal can be put at the cavity end where the signal is linearly polarized and the phase matching

conditions is satisfied, it is expected that the doubled frequency signal will be guided in the cavity and at the output end exhibited the same polarization as the original signal.

Also note that the current slope efficiency of the laser system is low, improving the pump coupling efficiency is desired in the future for more output power. In Figure 34 shows an updated design. This proposed design has one extra fiber section attached to the erbium fiber; L1 and L2 to be the same lens; angle cleave the erbium fiber end. The extra fiber section has core size and numerical aperture matched to the pump laser, also it is size is tapered down at one end to match the erbium fiber. In this way, it is expected the coupling efficiency would be significantly improved. The angle cleave of the Er fiber can reduce the parasite oscillations induced by ASE. The taping, splicing, and angle cleave can be done with the Vytran GPX 2000 fiber treating device available in the lab.

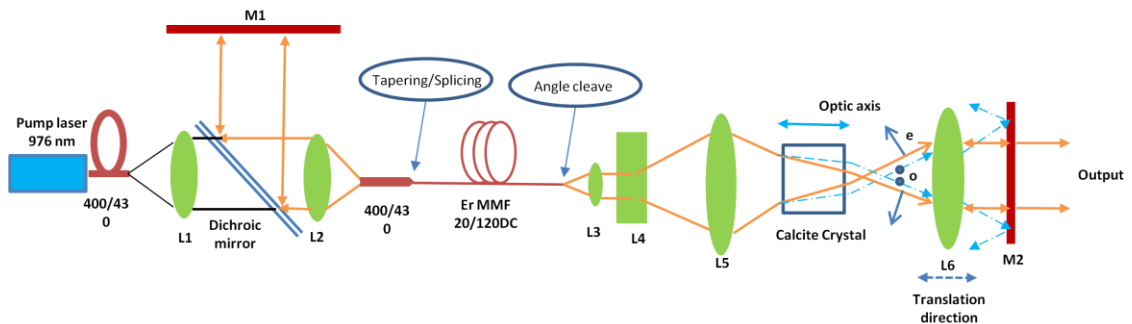


Figure 5-1. Updated fiber laser system design for further improve the slope efficiency.

BIBLIOGRAPHY

1. J. K. Sahu, Y. Jeong, D. J. Richardson, and J. Nillion, "A 103 W erbium-ytterbium co-doped large-core fiber laser," *Opt. Commun.* **227**, 159-163 (2003).
2. N. Park, P. Wysocki, R. Pedrazzani, S. Gribb, D. DiGiovanni, and K. Walker, "High-Power Er-Yb-Doped Fiber Amplifier with Multichannel Gain Flatness within 0.2 dB over 14 nm," *IEEE Photon. Technol. Lett.* **8**, 1148-1150 (1996).
3. L. Li, M. Morrel, T. Qiu, V. L. Temyanko, and A. Schülzgen, "Short cladding-pumped Er/Yb phosphate fiber laser with 1.5 W output power," *Appl. Phys. Lett.* **85**, 2721-2723 (2004).
4. D. Y. Shen, J. K. Sahu, and W. A. Clarkson, "High efficient Er, Yb-doped fiber laser with 188 W free-running and > 100W tunable output power," *Opt. Express* **13**, 4916-4921 (2005).
5. Y. Sintov, Y. Glick, T. Kopolovitch, and Y. Nafcha, "Extractable energy from erbium-ytterbium co-doped pulsed fiber amplifier and lasers," *Opt. Commun.* **281**, 1162-1178 (2008)
6. G. Canat, J-C. Mollier, and J-P. Bouzinac, G. M. Williams, B. Cole, and L. Goldberg, "Dynamics of high-power erbium-ytterbium fiber amplifier," *J. Opt. Soc. Am. B.* **22**, 2308-2318 (2005).

7. J. Nilsson, P. Scheer, and B. Jaskorzynska, "Modeling and Optimization of Short Yb³⁺-Sensitized Er³⁺-Doped Fiber Amplifier," IEEE. Photon. Technol. Lett. **6**, 383-385 (1994).
8. D. T. Nguyen, A. Chavez-Pirson, S. Jiang, and N. Peyghambarian, "A Novel Approach of Modeling Cladding-Pumped Highly Er-Yb Co-doped Fiber Amplifiers," IEEE J. Quantum Electron. **43**, 1018-1027 (2007).
9. H. Kogelnik, "On the propagation of Gaussian beam of light through lenslike media including those with a loss or gain variation," Appl. Opt. **4**, 1562-1569 (1965).
10. T. L. Paoli, "Waveguiding in a stripe-geometry junction laser," IEEE J. Quantum Electron., QE-13, **8**, 662-668 (1977)
11. L. W. Casperson, and A. Yariv, "The Gaussian mode in optical resonators with a radial gain profile," Appl. Phys. Lett. **12**, 355–357 (1968).
12. B. N. Perry, P. Rabinowitz, and M. Newstein, "Wave propagation in media with focused gain," Phys. Rev. A **27**, 1989–2002 (1983).
13. A. E. Siegman, *Lasers*, University Science Books, Mill Valley, CA (1986).
14. E. Siegman, "Propagating modes in gain-guided optical fibers," J. Opt. Soc. Am. A **20**, 1617-1628 (2003).
15. Y. Chen, V. Sudesh, T. McComb, M. C. Richardson, M. Bass, and J. Ballato, "Lasing in a gain-guided index anti-guided fiber," J. Opt. Soc. Am. B **24**, 1683-1688 (2007).
16. A. E. Siegman, Y. Chen, V. Sudesh, M. C. Richardson, M. Bass, P. Foy, W. Hawkins, and J. Ballato, "Confined propagation and near single-mode laser oscillation in a gain-guided, index antiguided optical fiber," Appl. Phys. Lett. **89**, 251101 (2006).

17. V. Sudesh, T. McComb, Y. Chen, M. Bass, M. C. Richardson, J. Ballato, and A. E. Siegman, "Diode-pumped 200 μm diameter core, gain-guided, index-antiguided single mode fiber laser," *Appl. Phys. B* **90**, 369-372 (2008).
18. T. Her, X. Ao, and L. W. Casperson, "Gain saturation in gain-guided slab waveguides with large-index antiguiding," *Opt. Lett.* **34**, 2411-2413 (2009).
19. H. S. Kim, and M. C. Richardson, "Output characteristics of a gain guided, index anti-guided fiber amplifier under the condition of gain saturation," *Opt. Express* **18**, 15969-15974 (2009).
20. O. Schmidt, J. Rothhardt, F. Röser, S. Linke, T. Schreiber, K. Rademaker, J. Limpert, S. Ermeneux, P. Yvernault, F. Salin, and A. Tünnermann, "Millijoule pulse energy Q-switched short-length fiber laser," *Opt. Lett.* **32**, 1551-1553 (2007)
21. J. Limpert, A. Liem, M. Reich, T. Schreiber, S. Nolte, H. Zellmer, A. Tünnermann, J. Broeng, A. Petersson, and C. Jakobsen, "Low-nonlinearity single-transverse-mode ytterbium-doped photonic crystal fiber amplifier," *Opt. Express* **12**, 1313-1319 (2004).
22. M. M. Vogel, M. Abdou-Ahmed, A. Voss, and T. Graf, "Very-large-mode-area, single-mode multicore fiber," *Opt. Lett.* **34**, 2876-2878 (2009).
23. J. Fini, "Design of solid and microstructure fibers for suppression of higher-order modes," *Opt. Express* **13**, 3477-3490 (2005).
24. A. E. Siegman, "Gain-guided, index-anti-guided fiber lasers," *J. A. Opt. Soc. Am. B* **24**, 1677-1682 (2007).
25. G. P. Agrawal, *Fiber-Optic Communication Systems*, John Wiley & Sons, Inc., New York, (2002).

26. G. P. Agrawal, *Nonlinear fiber Optics*, Academic, New York, (2001).
27. G. Nehmetallah, and P. P. Banerjee, "Stabilization of a (D+1)-dimensional dispersion-managed solutions in Kerr media by an alternating dispersion structure," *J. Opt. Soc. Am. B* **23**, 203-211 (2006).
28. L. Yu, M. Huang, and M. Chen, "Quasi-discrete Hankel transform," *Opt. Lett.* **23**, 409-411 (1998).
29. M. Guizar-Sicairos and J. Gutiérrez-Vega, "Computation of quasi-discrete Hankel transform of integer order for propagating optical wave fields," *J. Opt. Soc. Am. A* **21**, 53-58 (2004).
30. G. R. Hadley, "Transparent boundary conditions for beam propagation," *Opt. Lett.* **16**, 624-626 (1991).
31. S. T. Hendow, and S. A. Shakir, "Recursive numerical solution for nonlinear wave propagation in fibers and cylindrical symmetric system," *Appl. Opt.* **25**, 1759-1764 (1986).
32. G. Fibich, and A. L. Gaeta, "Critical power for self-focusing in bulk media and in hollow waveguides," *Opt. Lett.* **25**, 335-337 (2000).
33. C. Pollock, and M. Lipson, *Integrated Photonics*, Kluwer, Boston, MA (2003).
34. R. Ulrich, and G. Ankele, "Self-imaging in homogeneous planar optical waveguides," *Appl. Phys. Lett.* **27**, 337-339 (1975).
35. S. W. Allison, and G. T. Gillies, "Observations of and applications for self-imaging in optical fibers," *App. Opt.* **33**, 1802-1805 (1994).

36. L. B. Soldano, and E. C. M. Penning, "Optical Multi-Mode Interference Devices Based on Self-Imaging: Principle and Applications," *J. Lightwave Technol.* **13**, 615-627 (1995).
37. M. Fridman, M. Nixon, E. Ronen, A. A. Friesem, and N. Davidson, "Phase locking of two coupled lasers with many longitudinal modes," *Opt. Lett.* **35**, 526-528 (2010).
38. D. Pohl, "Operation of a Ruby Laser in the Purely Transverse Electric Mode TE_{01} ," *Appl. Phys. Lett.* **20**, 266-267 (1972).
39. Q. Zhan, "Cylindrical vector beams: from mathematical concepts to applications," *Adv. Opt. Photon.* **1**, 1–57 (2009).
40. C. Sun, and C. Liu, "Ultrasmall focusing spot with a long depth of focus based on polarization and phase modulation," *Opt. Lett.* **28**, 99–101 (2003).
41. P. Biss, and T. G. Brown, "Polarization-vortex-driven second-harmonic generation," *Opt. Lett.* **28**, 923–925 (2003).
42. S. Carrasco, B. E. A. Saleh, M. C. Teich, and J. T. Fourkas, "Second- and third-harmonic generation with vector Gaussian beams," *J. Opt. Soc. Am. B* **23**, 2134–2141 (2006).
43. P. Biss, K. S. Youngworth, and T. G. Brown, "Dark-field imaging with cylindrical-vector beams," *Appl. Opt.* **45**, 470–479 (2006).
44. F. Lu, W. Zheng, and Z. Huang, "Coherent anti-Stokes Raman scattering microscopy using tightly focused radially polarized light," *Opt. Lett.* **34**, 1870 (2009).

45. Q. Zhan, "Trapping metallic Rayleigh particles with radial polarization," *Opt. Express* **12**, 3377–3382 (2004).
46. H. Kawauchi, K. Yonezawa, Y. Kozawa, and S. Sato, "Calculation of optical trapping forces on a dielectric sphere in the ray optics regime produced by a radially polarized laser beam," *Opt. Lett.* **32**, 1839–1841(2007).
47. M. Meier, V. Romano, and T. Feurer, "Material processing with pulsed radially and azimuthally polarized laser radiation," *Appl. Phys. A* **86**, 329 (2007).
48. W. Cheng, J. W. Haus, and Q. Zhan, "Propagation of vector vortex beams through a turbulent atmosphere," *Opt. Express* **17**, 17829-17836 (2009).
49. J. W. Haus, Z. Mozumder, and Q. Zhan, "Azimuthal modulation instability for a cylindrically polarized wave in a nonlinear Kerr medium," *Opt. Express* **14**, 4757-4764 (2006).
50. A. A. Ishaaya, L. T. Vuong, T. D. Grow, and A. L. Gaeta, "Self- focusing dynamics of polarization vortices in Kerr media," *Opt. Lett.* **33**, 13-15 (2008).
51. A. Ishaaya, C. J. Hensley, B. Shim, S. Schrauth, K. W. Koch, and A. L. Gaeta, "Highly-efficient coupling of linearly- and radially-polarized femtosecond pulses in hollowcore photonic band-gap fibers," *Opt. Express* **21**, 18630-18637 (2009).
52. S. Sato, and Y. Kozawa, "Radially polarized annular beam generated through a second-harmonic-generation process," *Opt. Lett* **34**, 3166-3168(2009).

53. K. Yonezawa, Y. Kozawa, and S. Sato, "Generation of a radially polarized laser beam by use of the birefringence of a c-cut Nd:YVO₄ crystal," *Opt. Lett.* **31**, 2151–2153 (2006).
54. G. Machavariani, Y. Lumer, I. Moshe, A. Meir, S. Jackel, and N. Davidson, "Birefringence-induced bifocusing for selection of radially or azimuthally polarized laser modes," *Appl. Opt.* **46**, 3304–3310 (2007).
55. K. Yonezawa, Y. Kozawa, and S. Sato, "Compact laser with radial polarization using birefringent laser medium," *Jpn. J. Appl. Phys., Part 1* **46**, 5160–5163 (2007).
56. Y. Kozawa, and S. Sato, "Generation of a radially polarized laser beam by use of a conical Brewster prism," *Opt. Lett.* **30**, 3063–3065 (2005).
57. Q. Zhan, and J. R. Leger, "Interferometric measurement of Berry's phase in space-variant polarization manipulations," *Opt. Commun.* **213**, 241–245 (2002).
58. C. Rotschild, S. Zommer, S. Moed, O. Hershcovitz, and S. G. Lipson, "Adjustable spiral phase plate," *Appl. Opt.* **43**, 2397–2399 (2004).
59. G. Machavariani, Y. Lumer, I. Moshe, A. Meir, and S. Jackel, "Spatially-variable retardation plate for efficient generation of radially and azimuthally-polarized beams," *Opt. Commun.* **281**, 732–738 (2008).
60. A. K. Spilman, and T. G. Brown, "Stress birefringent, space-variant wave plates for vortex illumination," *Appl. Opt.* **46**, 61–66 (2007).
61. J. L. Li, K. I. Ueda, M. Musha, and A. Shirakawa, "Generation of radially polarized mode in Yb fiber laser by using a dual conical prism," *Opt. Lett.* **31**, 2969 (2006).

62. J. L. Li, K. I. Ueda, M. Musha, A. Shirakawa, and Z. M. Zhang, "Converging-axicon-based radially polarized ytterbium fiber laser and evidence on the mode profile inside the gain fiber," *Opt. Lett.* **32**, 1360 (2007).
63. J. L. Li, K. I. Ueda, A. Shirakawa, M. Musha, L. X. Zhong, and Z. M. Zhang, "39-mW annular excitation of ytterbium fiber laser with radial polarization," *Laser Phys. Lett.* **4**, 814 (2007).
64. M. Fridman, G. Machavariai, N. Davidson, and A. A. Friesem, "Fiber lasers generating radially and azimuthally polarized light," *Appl. Phys. Lett.* **93**, 191104 (2008).
65. A. Ghatak, and K. Thyagarajan, *An Introduction to Fiber Optics*, Cambridge University Press, Cambridge (2008)
66. W. T. Silfvast, *Laser fundamentals*, Cambridge University Press, Cambridge (2004).
67. S. Huard, *Polarization of light*, John Wiley & Sons, New York (1997).
68. K. Otsuka, S.-C. Chu, C.-C. Lin, K. Tokunaga, and T. Ohtomo, "Spatial and polarization entanglement of lasing patterns and related dynamic behaviors in laser-diode-pumped solid-state lasers," *Opt. Express* **17**, 21615-21627 (2009).
69. G. Volpe, D. Petrov, "Generation of cylindrical vector beams with few-mode fibers excited by Laguerre–Gaussian beams," *Opt. Commun.* **237**, 89–95 (2004).